Biol Cybern
DOI 10.1007/s00422-014-0634-2

ORIGINAL PAPER

Biological Cybernetics

Multidimensional gain control in image representation and processing in vision

S. Furman · Y. Y. Zeevi

Received: 5 November 2012 / Accepted: 20 October 2014

Abstract A generic model of automatic gain control (AGC) is proposed as a general framework for multidimensional automatic contrast sensitivity adjustment in vision, as well as in other sensory modalities. We show that a generic feedback AGC mechanism, incorporating a nonlinear synaptic interaction into the feedback loop of a neural network, can enhance and emphasize important image attributes, such as curvature, size, depth, convexity/concavity and more, similar to its role in the adjustment of photoreceptors and retinal network sensitivity over the extremely high dynamic range of environmental light intensities, while enhancing the contrast. We further propose that visual illusions, well established by psychophysical experiments, are a by-product of the multidimensional AGC. This hypothesis is supported by simulations implementing AGC, which reproduce psychophysical data regarding size contrast effects known as the Ebbinghaus illusion, and depth contrast effects. Processing of curvature by an AGC network illustrates that it is an important mechanism of image structure pre-emphasis, which thereby enhances saliency. It is argued that the generic neural network of AGC constitutes a universal, parsimonious, unified mechanism of neurobiological automatic contrast sensitivity control. This mechanism/model can account for a wide range of physiological and psychophysical phenomena, such as visual illusions and contour completion, in cases of occlusion, by a basic neural network. Likewise, and as important, biologically motivated AGC provides attractive new means for the development of intelligent computer vision systems.

S. Furman (✉) · Y. Y. Zeevi
Department of Electrical Engineering, Technion—Israel Institute of Technology, 32000 Haifa, Israel
e-mail: shaifurman@yahoo.com

Y. Y. Zeevi
e-mail: zeevi@ee.technion.ac.il

Keywords Computer vision · Computational models of vision · Filtering enhancement · Projections · Multidimensional image representation · Size and shape · Depth cues · Neural nets models

1 Introduction

The perceived image is quite different from the original image projected onto the retina. Some of the image features that are of great importance (biologically speaking) are enhanced, whereas other that are less significant are barely noticed or even ignored (i.e., suppressed). Many examples of this selective enhancement/suppression phenomenon exist. Usually they are referred to as "visual illusions" (see Fig. 1 for such examples). This type of visual illusion can be explained by the way the human visual system (HVS) generally processes visual information, implementing nonlinear adaptive gain control (AGC) mechanisms. For other visual illusions, there exist alternative, qualitative, theories (Gregory 2009). Understanding the organization and functioning of visual systems is obviously of great importance in the field of neurobiology. This is primarily due to our curiosity to better understand the structure and function of the brain. But, it is likewise important in the field of image processing and computer vision because of its potential use in the design of intelligent systems that mimic biological vision (for such examples, see Yang et al. 2009; Tran et al. 2009). By matching image presentations to the known performance of the visual system, more meaningful and efficient communication can be achieved (Zeevi and Kronauer 1985). After all, most of the information generated for human consumption is communicated with the human observer via the visual system as the final receiver. In yet another way, image processing modeled after the visual system may prove to be important in

Published online: 21 November 2014

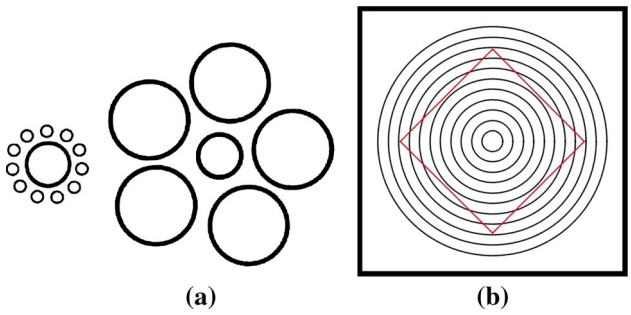

Fig. 1 Effects of size (**a**) and curvature (**b**) contrast. **a** *Both circles* in the *middle* are of the same size. **b** The *square's boundaries* are *straight lines*, but they are perceived as being curved

machine vision. And of course, now that visual prosthetics are becoming a workable reality (Koch et al. 2008; Palanker) this understanding is essential. Moreover, such an understanding may lead to the development of an image metric accounting for human perception. This should contribute to further advancement of recognition and classification algorithms.

Gibson (1937) had claimed that adaptation and negative after-effect are to be conceived as a process of adjustment and readjustment of the physical-phenomenal correspondence of a certain type of sensory dimension, under the influence of a tendency for sensory activity to become normal, standard or neutral. He noticed that this similarity cuts across the sensory modalities of our world, including pressure, size, distance, temperature, brightness, curvature (convex–concave), and other modalities and dimensions.

Zeevi and Mangoubi (1978) showed that adaptation plays an important role in the suppression of quantal and receptor internal noise. Wainwright (1999) proposed that visual adaptation in orientation, spatial frequency and motion can be understood from the perspective of optimal information transmission. Ullman and Schechtman (1982) had claimed that adaptation and gain control can fulfill two useful functions: correction of errors and recalibration. In the multichannel mode of the spatial case, the gain control maintains the overall sensitivity of the system: If the gain of one of the channels increases, the gain of neighboring channels decreases and vice versa.

Automatic gain control (AGC) has been widely used to account for many sensory adaptation phenomena. Shefer and Zeevi considered it in the context of intensity adaptation (Shefer 1979; Zeevi and Shefer 1981), Weltsch for contrast adaptation in the primary visual cortex (Weltsch-Cohen 2002), Ding and Sperling for contrast adaptation of the "cyclopean" image (Ding and Sperling 2006) and Lu and Sperling for contrast adaptation in motion detection (Lu and Sperling 1996; Croz and Rushton 1966; Krauskopf and Mollon 1971) for chromatic adaptation, Shapley and Enroth-Cugell for retina adaptation (Shapley and Enroth-Cugell 1984; Schwartz and Simoncelli 2001) for either visual or auditory adaptation. It is therefore natural and tempting to implement the AGC model in processing images which incorporate some other less-investigated dimensions of adaptation, such as size, depth and curvature, in processing of images. Likewise, such an investigation may facilitate our understanding of how adaptation along these dimensions takes place in the visual system (or other sensory modalities for this matter).

The purpose of this study is to analyze adaptation along less-investigated image dimensions and process these image attributes by means of the AGC model in order to mimic the human visual system (HVS), and thereby infer that there exists a unified neurobiological framework of sensory information processing. Such a framework considered in the context of vision (biological and computer-based alike) can be also implemented in advanced image-processing algorithms that highlight various features and image structures. Such a multidimensional adaptive framework of image processing can then be implemented in intelligent image processing and computer vision systems, similar to the high dynamic range camera that mimics the eye (Ginosar et al. 1992; Zeevi et al. 1995); an implementation that has become the gold standard of cameras and other image acquisition systems. The performance of the proposed multidimensional AGC framework of image processing is tested by computer simulations, for each dimension separately, and is compared to the results of psychophysical experiments.

Inferring from what is known about retinotopic projections onto the visual cortex, we consider the gain control-based processing of image attributes to be executed independently of each other. Clearly, the independency assumption is not always valid. It is therefore instructive to highlight an alternative approach, introduced in the context of image processing and computer vision (Kimmel et al. 2000; Sochen and Zeevi 1998), which is attractive for modeling of visual projection onto and processing in a multidimensional visual space. This alternative approach considers the embedding of an image manifold in a higher-dimensional-combined position (spatial)-feature space. Features such as color, curvature and size, mentioned above, constitute in this representation the image attributes (to which we refer also as visual dimensions). Sensitivity adjustment by means of nonlinear gain control is executed in this case in the multidimensional space in a unified coherent manner. Although this approach is not in the scope of the present work and will be dealt with elsewhere, we indicate along the manuscript how it can be incorporated.

2 The basics of visual AGC framework

The proposed AGC model of visual adaptation is based on the original work of Shefer (1979), Zeevi and Shefer (1981) and

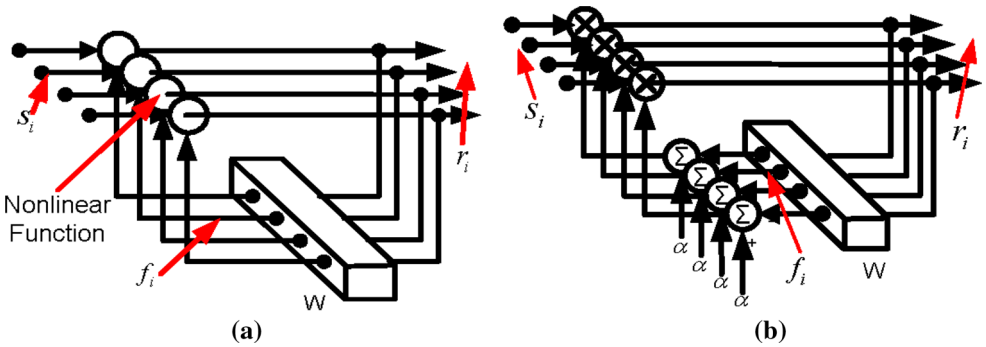

Fig. 2 **a** Core of sensory AGC model. **b** Schematic diagram of a specific embodiment of the generic AGC processor, where the nonlinear interaction in the feedback loop is implemented by a multiplier

on the subsequent development of the adaptive sensitivity camera that mimics the eye (Ginosar et al. 1992; Zeevi et al. 1995). The model has been motivated by the structure and function of the retina and, in particular, by its high spatiotemporal sensitivity to small changes in intensity accomplished over extremely high dynamic range. According to this nonlinear AGC adaptation model, the output of a receptor or of a subsequent processing cell is adjusted by subtracting from its input a nonlinear function of its input and a feedback signal, which constitutes a local weighted sum of the outputs (Fig. 2a):

$$r_i = \alpha \cdot s_i - T(s_i, f_i), \tag{1}$$

where r_i is the output (or response) of cell i, s_i is the input (W in Fig. 2a is the weighting of a feedback operator (matrix)), f_i is the feedback (see (3)), α is a fixed forward gain, and T is a nonlinear input–output-feedback interaction function. The crucial ingredient of this AGC model is the nonlinearity within the local feedback loop (i.e., the function T). This is a fundamental extension of the lateral inhibition (i.e., linear output convolution) feedback model into the nonlinear regime, presumed to be biologically mediated by the retinal interplexiform cells and/or similar structures in other loci along the processing pathway, and/or other sensory networks. It is important to note that qualitatively T may assume a wide range of nonlinear functions and, yet, the feedback loop in which such nonlinear function is embedded will exhibit functional AGC (see Ohlson 1974; Snippe and Hateren 2007 for such examples). It is in particular interesting to note in this context the feedforward-and-feedback model of visual adaptation, wherein Sperling (1970) implements a so-called shunting synaptic inhibition (see Furman 1965).

If we assume that the cells (pixels processing units) are small and close enough, we can model the feedback operator by a continuous function and use convolution to represent the action of W on the output. Extending the proposed AGC framework to other image dimensions (attributes), each of the functions of x is a dependent variable that stands for an image attribute such as curvature, size and depth. In this case, (1) is written as:

$$r(x) = \alpha \cdot s(x) - T(s(x), f(x)), \tag{2}$$

where $s(x)$ and $r(x)$ are the input and output of an image attribute at the two-dimensional spatial position, x, respectively. This is attributed, as noted, to nonlinear synaptic mechanisms such as those that exist in the retinal outer plexiform layer and in the visual cortex. In a specific embodiment of this general conceptual model, the nonlinear component is a multiplier (Fig. 2b). The model is then comprised of a series of static instantaneous multipliers, one for each foveal receptor channel, that multiply the inputs of the channels with the outputs of the feedback. The feedback is calculated by subtracting the output of the local operator W from a constant value. The operator W is a local averaging operator (in space).

In the continuous model, the feedback $f(x)$ is obtained by a convolution of W with the output $r(x)$:

$$f(x) = \int r(x')\mathrm{W}(x - x')dx'. \tag{3}$$

The AGC model output (derived from (2)) for multiplicative synaptic inhibition is given by:

$$r(x) = s(x)\left[\alpha - \left|\int r(x')\mathrm{W}(x - x')dx'\right|\right]. \tag{4}$$

The function of the feedback is to position the enhancement mechanism, high gain operating curve, symmetrically around the local operating point. W can be chosen as exponent, Gaussian, triangle, rectangular or any other symmetric kernel for which one can obtain the qualitative characteristics of the AGC. The quantitative behavior will, of course, depend on the specific choice of W.

The operator (4) has a unique solution for

$$\max_x\{|s(x)|\} < \frac{1}{S_\mathrm{W}}, \tag{5}$$

where S_W is:

$$S_W = \int W(x)dx. \tag{6}$$

See Appendix 1.

These conditions can be extended using the discrete form of W:

$$w_i > 1; \qquad \sum_{j \neq i} |w_j| < 1. \tag{7}$$

2.1 Small signal analysis

Although we are concerned in general with "large signal" performance of the visual AGC, it is nevertheless useful to perform also small signal analysis of the model. We note that the case of small signal is also of interest from the viewpoint of visual function. Although the visual system (or any image acquisition system) is exposed to an extremely wide dynamic range of intensity, at any specific time and/or position the intensity varies only over a relatively narrow range of intensities.

For the small signal analysis, we assume that both the output and the input of the model are comprised of a "local DC" modulated by a small AC signal component:

$$\tilde{S}(x) = C_s + s(x); \qquad \tilde{R}(x) = C_r + r(x), \tag{8}$$

$$\int s(x)dx = 0; \qquad \int r(x)dx = 0. \tag{9}$$

Alternatively, due to the narrow range of intensities, one may use Weber's contrast:

$$\tilde{S}_B(x) = \frac{C_s + s(x)}{C_s} = 1 + \frac{s(x)}{C_s}. \tag{10}$$

For simplicity, we assume also that W is a rectangular function. Under these assumptions, (3) yields:

$$f(x) = \int_{\Omega} \tilde{R}(x')W(x - x')dx' = \int_{\Omega} \tilde{R}(x')dx' = C_r, \tag{11}$$

where Ω is the integration region, limited by the width of W.

Substituting (8), (9) and (11) for the corresponding variables in (4) yields:

$$r(x) = s(x)\frac{\alpha}{1 + C_s}\ ; C_r = \frac{\alpha \cdot C_s}{1 + C_s}. \tag{12}$$

Equation (12) expresses a sigmoidal function for the AC response, which is closely related to Weber law of sensory perception. The latter implies that the system gain is inversely proportional to the sensory input's local DC. Examining the local DC response (C_r) reveals a highly compressive response curve that never exceeds the value of "1" (see Fig. 3a)—black line). This means that the response does not saturate in a noticable manner, and yet, for each local DC value, the system exhibits high sensitivity (see Fig. 3a—red lines depicting a sequence of AC response curves for various values of local DC).

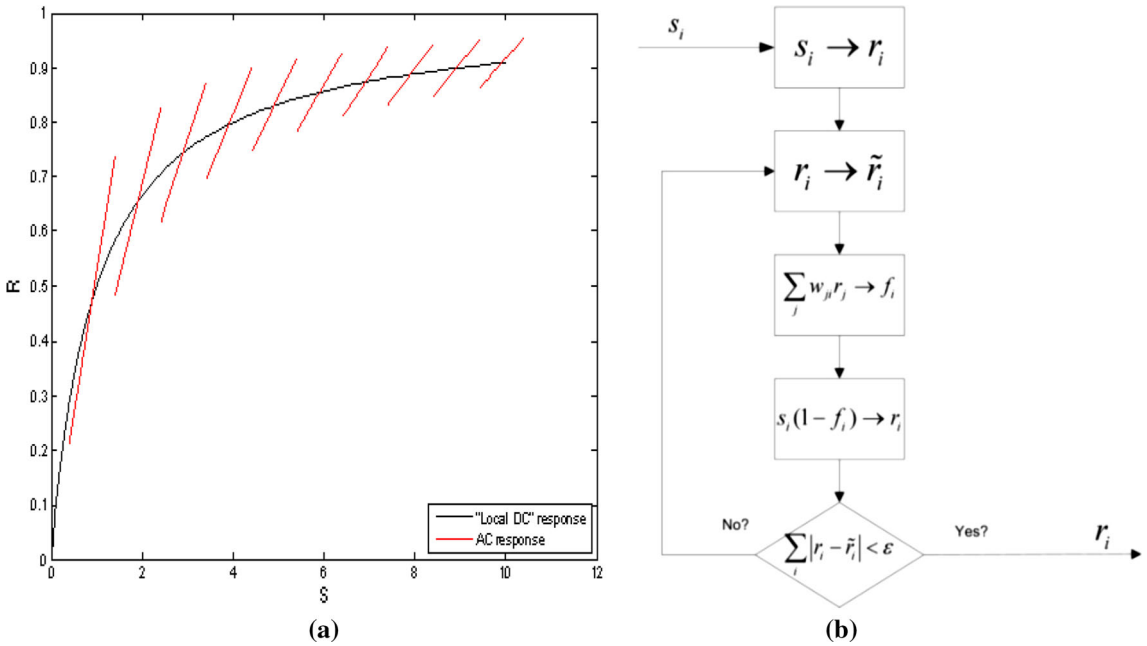

Fig. 3 **a** Small signal response. The AC, r(x), (*in red*), is shown superimposed on the "local DC," C, response (*in black*). **b** Flowchart for calculating the visual AGC response to some arbitrary input (color figure online)

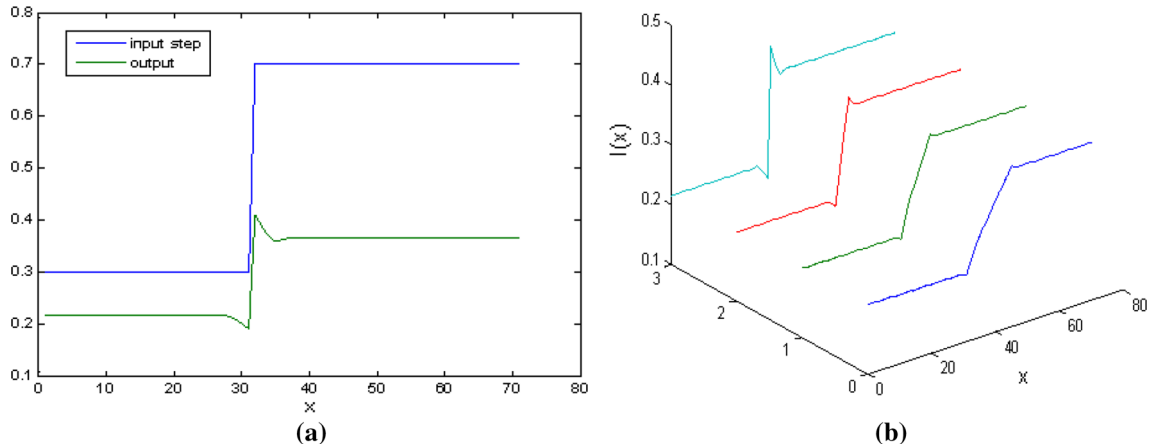

Fig. 4 **a** Step response of the AGC model, superimposed on a step stimulus. **b** AGC model responses to various ramp slopes. Note the increase in overshoot and undershoot with the increase in slope steepness

Weber law is characteristic of all sensory modalities, including weight, vision, touch and sound.

2.2 Simulations

In its discrete form, (4) exhibits the complexity of a many body problem. To obtain a closed form solution for some arbitrary input is a major challenge, not yet dealt with. Therefore, we employ a numeric solution of an iterative process. Figure 3b presents the flowchart of the algorithm for numeric solution of the AGC model. The solution is unique, provided the process converges (Shefer 1979; Zeevi and Shefer 1981).

2.3 Step response

We now explore two of the main functional features of the models—adaptation (i.e., reduction in gain for spatially constant stimulus) and edge enhancement—by examining the step/ramp response of the models. The step/ramp response is of special interest, since steps occur in natural stimuli (Griffin et al. 2004) and are often used to study the dynamics of adaptation. Figure 4a depicts step response of the nonlinear AGC model, superimposed on the step input. This example highlights the main characteristics of the model:

Adaptation: The response adapted to a constant input is decreased, while high values are affected more than lower values. This reflects the compression of a wide dynamic range of the input.

Edge enhancement : The relative contrast is increased. This is caused by the overshoot and undershoot of the response. Note that due to the nonlinearity of the model, the overshoot is more pronounced than the undershoot as is indeed observed experimentally (i.e., perceptually). Both of the overshoot and undershoot depend on the slope of the input ramp (Fig. 4b). When the input represents intensity, this phenomenon of overshoot/undershoot is well known as "Mach bands" (Ratliff 1965).

2.4 Noise and SNR analysis

Various types of noise are encountered in vision and imaging systems, e.g., the quantal noise and the neural noise (for more details see Mangoubi 1979), or imaging detector noise. To assess the effect of the AGC on SNR, we adopt the common assumption that the noise is additive and has zero mean and small variance σ_s^2 compared with the signal:

$$S_n(x) = s(x) + \eta_s(x), \tag{13}$$

where $s(x)$ is the noise-free input, $\eta_s(x)$ the noise of the source (input), and $S_n(x)$ is the noisy input.

We are mainly concerned in the context of the noise and SNR analysis with input that is locally constant.

Observing the similarity of (13) and (8) suggests that we may analyze the effect of the noise using the same analysis employed in the case of the small signal, where the input signal is analogous to C_s, and the noise is analogous to $s(x)$. In the latter case, the output noise is:

$$\eta_r(x) = \eta_s(x)\frac{\alpha}{1+s(x)}. \tag{14}$$

Equation (14) implies that the average and variance of the output noise are:

$$\mu_r = \frac{\alpha}{1+s(x)}\mu_s = 0; \qquad \sigma_r^2 = \left(\frac{\alpha}{1+s(x)}\right)^2 \sigma_s^2 \tag{15}$$

indicating that the variance of the noise at the output of a neural channel implementing the feedback AGC output noise

depends on the input signal. It depicts noise suppression as a function of the input intensity, consistent with neurophysiological measurements and psychophysical results (see, e.g., Zeevi and Mangoubi 1978; Faisal et al. 2008 for more details).

Note that the above analysis does not postulate any assumptions regarding characteristics of the noise (such as higher moments and/or distribution) besides small signal assumption.

Alternatively, the variance of the output noise can be evaluated as follows (Papoulis 1965):

$$\sigma_r^2 \cong \left[g'\left(\bar{\eta}_s\right)\right]^2 \sigma_s^2, \tag{16}$$

where $r = g(s)$ is a smooth monotonic function of s, σ_r^2 is the variance of the response, σ_s^2 is the variance of the input, and $\bar{\eta}_s$ is the average of the input. In the case of additive noise, the input can be written as in (13), implying that the input consists of a noise-free component $s(x)$ and noise with a zero mean. We obtain an explicit form by using the discrete form, yielding the response of cell (or neural channel) i as a function of the input to this cell, and the responses of the other cells (see (18)). Therefore,

$$\sigma_{r_i}^2 \cong \left[g'\left(\bar{\eta}_{s_i}\right)\right]^2 \sigma_{s_i}^2, \tag{17}$$

$$r_i = g\left(s_i\right) = \frac{s_i\left(\alpha - \sum_{j\neq i} w_j r_j\right)}{1 + s_i w_i}, \tag{18}$$

$$\begin{aligned} g'\left(s_i\right) &= \frac{\partial r_i}{\partial s_i} \\ &= \frac{\left(\alpha - \sum_{j\neq i} w_j r_j\right)\left(1 + s_i w_i\right) - s_i w_i\left(\alpha - \sum_{j\neq i} w_j r_j\right)}{\left(1 + s_i w_i\right)^2} \\ &= \frac{\left(\alpha - \sum_{j\neq i} w_j r_j\right)}{\left(1 + s_i w_i\right)^2}. \end{aligned} \tag{19}$$

Assuming that $g\left(s\right)$ is a smooth function of s, the variance is:

$$\sigma_{r_i}^2 \cong \left[\frac{\left(\alpha - \sum_{j\neq i} w_j r_j\right)}{\left(1 + \bar{\eta}_{s_i} w_i\right)^2}\right]^2 \sigma_{s_i}^2. \tag{20}$$

Equation (20) shows, again, that the response variance is inversely proportional to the input average $\bar{\eta}_{s_i}$.

Note that again, this analysis does not necessitate any restrictive assumptions regarding noise characteristics. Only the first two moments are required.

We can define the SNR characteristics of the system as:

$$\mathrm{SNR} = \frac{\mathrm{signal}^2}{\sigma^2} = \frac{\tilde{C}_m^2}{\sigma^2}, \tag{21}$$

where $\tilde{C}_m$ is the Michelson contrast:

$$\tilde{C}_m = \frac{I_{\max} - I_{\min}}{I_{\max} + I_{\min}}, \tag{22}$$

$I_{\max}$ and $I_{\min}$ being the highest and the lowest intensity values (i.e., peak and trough), respectively. Note that in the case of the response, the calculated maximum and minimum values include the overshoot and undershoot.

For a general step input (i.e., sharp, one-dimensional edge in the case of an image),

$$s(x) = a_1 + a_2 U(x), \tag{23}$$

where a_1 is the lower constant value (intensity) of the step and $a_1 + a_2$ is the upper constant (intensity) value, the SNR is improved by:

$$\frac{\mathrm{SNR}_r}{\mathrm{SNR}_s} = \left(\frac{1 + a_1 + a_2}{\alpha}\right)^2 \quad \text{or} \quad \left(\frac{1 + a_1}{\alpha}\right)^2, \tag{24}$$

where the two alternative measures of SNR noise improvement are related to the noise at the upper part or lower part (left) of the step (edge), respectively. It is interesting to observe that the SNR improvement is equal exactly to the noise suppression factor of the AGC model. This is due to the fact that the contrast of the input signal is equal to the contrast of the response.

3 The effect of biological sensory AGC on processing and perception along curvature/size/depth and convex–concave dimensions

3.1 Background

3.1.1 Overview of differential geometry

To establish the context in which curvature processing is formulated, it is useful to review a few elementary notions adopted from differential geometry. The review is focused on curves in the plane, but the results can be generalized to higher dimensional (see, e.g., Do Carmo 1976 for more details).

Let I be an interval in one-dimensional Euclidean space E^1. A curve C is defined as a continuous mapping $x : I \rightarrow E^2$ from the interval to the plane, where

$$x\left(\lambda\right) = \left(x_1(\lambda), x_2(\lambda)\right). \tag{25}$$

A curve may be reparameterized in terms of its arc length s:

$$x\left(s\right) = \left(x_1(s), x_2(s)\right). \tag{26}$$

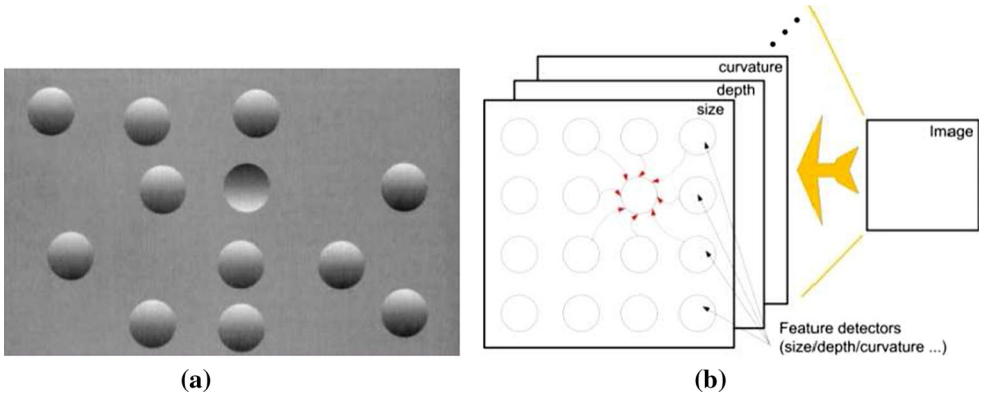

Fig. 5 **a** An example of a display, used in testing search for targets defined by depth cues. The target "pop-up"s from the distractors with little effect of the number of distractors. **b** The generalized retinotopic mapping concept: The HVS consists of multiple networks of cells that create multiple projections along image dimensions, wherein neighboring regions of the image are preserved by neighboring regions of the visual map

The curvature κ is then defined as rate of change in orientation per unit arc length:

$$x''(s) = (x_1''(s), x_2''(s)) = \kappa n$$

or

$$\kappa = \frac{x_1'(\lambda)x_2''(\lambda) - x_1''(\lambda)x_2'(\lambda)}{(x_1'(\lambda)^2 + x_2'(\lambda)^2)^{3/2}}, \tag{27}$$

while the geometric interpretation for the curvature is the curve radius:

$$\mathrm{R} = \frac{1}{\kappa}. \tag{28}$$

3.1.2 Locality and parallelism of curvature, size and depth

A key fact regarding the structural and functional organization of the HVS (which supports our AGC model) is that processing along image dimensions of size, curvature, depth and/or other dimensions is performed locally and in parallel over the entire image (Hochstein and Ahissar 2002). These image dimensions are believed to correspond to "elementary features" (Cavanagh et al. 1990; Wolfe et al. 2003) of image representation in the HVS. Consequently, the image is decomposed along a number of dimensions and into a number of separable components.

This concept had been tested in many psychophysical experiments such as "pop-up" experiments. In these experiments, there is a target with a unique feature which is not shared by the distractors. If the feature is detected early along the visual pathway, and if visual processing is performed locally and in parallel, the target should "pop-up" from the distractors with little effect of the number of distractors. Treisman and Gormican (1988) showed that such "pop-up"s are asymmetric in that some features are detected more easily when they are present rather than when they are absent, which implies that the processing is nonlinear. Figure 5a presents an example of such experiment for target defined by convexity/concavity depth cues (see Enns and Rensink 1990a, b). We may conclude that size, curvature and depth are processed locally and in parallel.

3.1.3 Adaptation and feature detectors

It is well known that prolonged inspection of a curved line causes adaptation to curvature (e.g., the curvature after-effect Gibson 1937; Coltheart 1971). Such after-effects are believed to reflect a change in the sensitivity of neurons that encode the adapted feature and, thus, imply the existence of neurons that act as detectors of that feature (Hancock and Peirce 2008).

Whereas curvature detection and representation were popular in vision research some time ago (Riggs 1973; Stromeyer and Riggs 1974; Watt 1984), there only a few recent findings in support of curvature importance in biological vision. Of these we wish to single out the work of Zucker and his associates (Dobbins et al. 1987; Parent and Zucker 1989; Zucker et al. 1988). Curvature representation and processing is, however, important in pattern recognition algorithms of computer vision (Parent and Zucker 1989; Monroy et al. 2011; Farzin and Suomela 1998; Lawlor and Zucker 2013). Indeed, based on earlier studies, some investigators agree that curvature detectors are present along the early stages of the visual pathway (Riggs 1973; Stromeyer and Riggs 1974). In several of these studies, it has been shown how such curvature calculations can be estimated by convolution with certain reasonable receptive fields of neural cells (Koenderink and Doorn 1987; Dobbins et al. 1987). For example, Wilson et al. have shown

how global curvature information can be extracted from local detectors using concentric glass patterns (Wilson et al. 1997).

Sutherland (1968) concluded that many species have the capacity to classify a shape as the same shape regardless of changes in size, at least over a considerable range, and that this capacity is innate. This ability can be considered as irrelevance of the absolute ("DC") component of size information and relevance of changes in size only.

Blakemore and Campbell (1969) suggested that the human visual system may possess neurons selectively sensitive to size. They also hypothesized that this neural system may play an essential preliminary role in the recognition of complex images. Carey et al. (1996) suggested that size, motion and orientation measures are processed in parallel by the dorsal stream mechanisms.

The visual system perceives depth based on several cues such as stereoscopic views, motion parallax, object size, object translation and rotation. Hubel and Wiesel (1970) have identified cells that are involved in depth information representation from stereoscopic vision. A number of authors have reported simultaneous depth-contrast effects for stimuli defined by stereoscopic, motion parallax and other cues (see Curran and Johnston 1996; Graham and Rogers 1982).

Existence of adaptation and contrast effect of a specific feature is closely related to the existence of detectors of this feature (or a specific channel). Adaptation and contrast effects are well documented with reference to curvature, size and depth. It, therefore, seems reasonable to assume that curvature, size and depth information are processed over the entire image (in parallel), by neural structures wherein each cell (or group of cells) corresponding to a specific location represents local feature information.

3.1.4 Retinotopic mapping along all image dimensions

The concept of retinotopic mapping was elaborated by Hubel and Wiesel (1968) within the context of visual orientation representation. We expend this concept with reference to additional image dimensions (curvature, size, depth, color, etc.) and generalize it by assuming that the HVS consists of multiple networks of cells that create multiple projections along image dimensions, wherein neighboring regions of cells preserve the neighborhood regions of the feature in the image. Figure 5b depicts this generalized concept. The HVS consists of multiple networks, one for each image dimension—size, color, curvature, etc. Each network consists of many feature detectors. Each detector is location specific. Together these detectors cover the entire image and form a network that projects the image along a specific dimension.

It is assumed that these networks incorporate the generic sensory AGC FB loop. Thus, processing along each image dimension in vision (or any dimension of other sensory modalities for this matter) can be modeled by AGC.

Two of these visual dimensions deserve a special attention. These are the curvature and size features. Curvature is represented as a discrete set of curvature values, as defined in Sect. 3.3.1. Representation of size of discrete objects is assigned to the centers of the objects.

Alternatively, one can incorporate processing in a higher-dimensional space, in which a curve is considered to be a vector associated with the spatial coordinates (x, y), incorporating both the geometric curvature of (28) and its angular orientation defined by the angle perpendicular to the tangent of the curve at the point of the curvature. Thus, a curve in a planar image is considered to be a two-dimensional surface embedded in a four-dimensional space whose coordinates are $(x, y, \kappa, \vartheta)$, where κ denotes the curvature and ϑ the angle of orientation of the curvature. The curvature AGC in vision, or in computer vision, is then applied in this 4D space to obtain a cortical output in a curvature map for the purposes of high-level vision, or in computer vision. This curvature map does not have to be necessarily back-projected onto the image space to obtain the resultant curve, as would be required in image-processing applications. If one considers the continuous gray-level image rather than the contours, it is envisioned in the context of this paper to be a three-dimensional surface, $(I(x, y))$, where I is the intensity or contrast, embedded in a four-dimensional space of (x, y, I, Ψ), where Ψ denotes the convexity/concavity dimension. Unlike the curvature, the convexity/concavity dimension assumes values other than zero at each (x, y) where the gray-level gradient is not equal to zero.

The size map (dimension) is considered as a two-dimensional surface, $\sigma(x, y)$, embedded in a three-dimensional space whose coordinates are (x, y, σ), similar to the embedding of the curve in the four-dimensional space of the curvature map.

3.2 Visual illusions indicative of AGC processing

Two psychophysical experiments are considered in the sequel as examples illustrating the effects of AGC. The first is the size-contrast effect (the Ebbinghaus illusion), while the second is concerned with the depth-contrast effect. It is shown that the AGC model/algorithm reproduces the illusions.

3.2.1 Size contrast

The Ebbinghaus illusion is commonly used as an example of a simple size-contrast effect. In this illusion, the apparent size of a central target is affected by a ring of surrounding inducers. Figure 1a illustrates a well-known setup that induces this illusion, as it most often appears in general textbooks. This form is typically used to illustrate a simple size-contrast

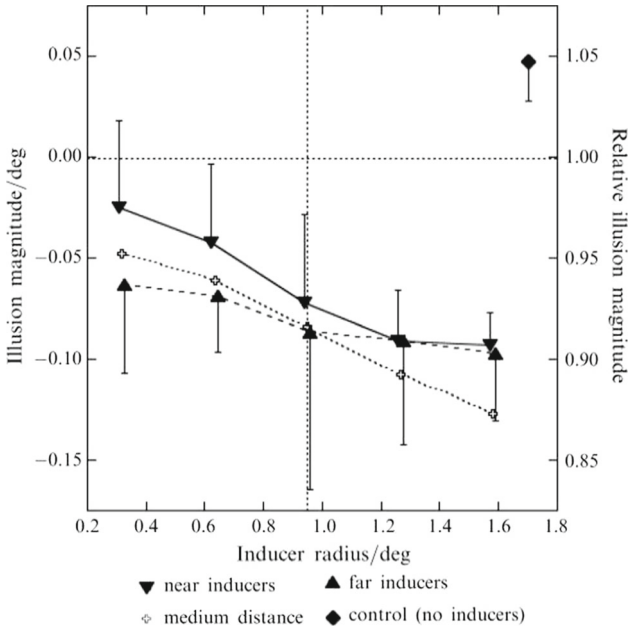

Fig. 6 Results of the Ebbinghaus illusion experiment [adopted from Roberts et al. (2005)] showing that apparent size of the target is reduced as the inducers get bigger, consistent with a size-contrast effect. The effect is further emphasized when the inducers are at larger distances

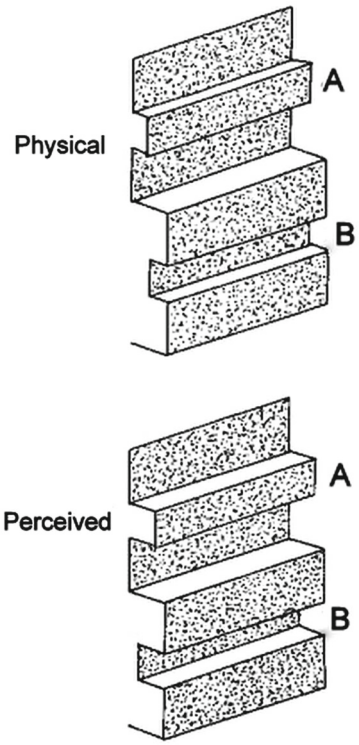

Fig. 7 Depth-contrast effect [adopted from Graham and Rogers (1982)]: *bar A* is perceived as lying above *bar B*, although they are physically at the same depth

effect, in which large inducers make the target appear smaller while small inducers make it appear larger.

Roberts et al. (2005) have further investigated the above effect and concluded that it arises from a number of factors that include the relative size of the inducers (compared with that of the target), the number of inducers and their distance from the target. These authors found that the apparent size of the target is reduced more efficiently when the inducers get bigger and at larger distances (see Fig. 6).

3.2.2 Depth contrast

Graham and Rogers (1982) have shown depth-contrast effect perceived from motion parallax and stereoscopic information. The perceived effect is illustrated in Fig. 7. The perceived depth is affected by the surrounding, and so, although bar A and bar B are at the same physical depth, they are perceived as though bar A is above bar B.

3.3 Simulation results

We assume that visual information is represented in a multidimensional image space, but do not address the issue of how this information was extracted, or projected onto this space. This assumption is reasonable, since many techniques/visual models of depth/size/curvature (or other image dimensions) estimation are available. [For an example of curve estimation, see Parent and Zucker (1989) and Zucker et al. (1988).]

3.3.1 Curvature processing

In order to provide an intuitive understanding of what is the effect of AGC on curvature, i.e., what is the input–output relationship insofar as the shape of the curve is concerned, we implement for the sake of simplicity a one-dimensional algorithm. The original curve is assumed to consist of discrete points $(x_1, y_1) \cdots (x_n, y_n)$. Curvature is calculated at each point along the curve yielding the corresponding set of discrete set of curvature values $(\kappa_1, \cdots, \kappa_n)$, as described in Appendix 2. The generic input to the AGC operator, $s(x)$, assumes in this case the form of curvature vector, $\kappa(l)$, where l denotes the position of the curvature value along the vector. The generic output $r(x)$ becomes now a 1D curvature vector of the resultant curve, which is used in turn in the reconstruction of the output/perceived/response curve, constructed according to the algorithm presented in Appendix 2, i.e., each point is calculated according to the previous point and a circular segment defined by the corresponding curvature. In this case, spatial correspondence between the input and output is lost.

Two curves are considered as examples of curvature processing by neural AGC. The first one is a curve with constant curvature, i.e., a section of a circle (Fig. 8). Note that since the curvature is constant, its extent is reduced as

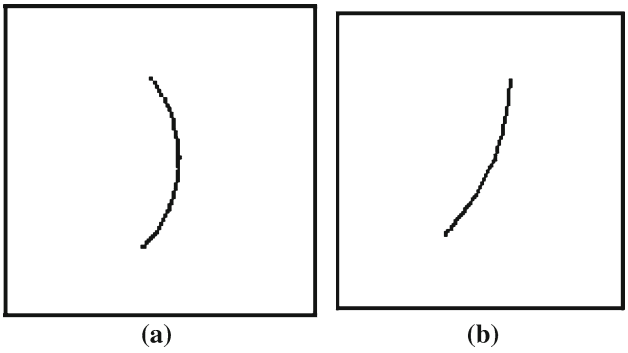

Fig. 8 Results of AGC processing of constant curvature, illustrating reduction in curvature ("adaptation"). **a** is the original curve (i.e., the input to the system), and **b** is the result of (**a**) being processed by the AGC neural network. The extent of curvature left in the adapted curve (**b**) depends on the AGC parameters, similar to the DC left in the processing of an edge in the case of a spatial step input. Note that due to the 1D implementation of the AGC along the curve, spatial correspondence between the input, (**a**), and output, (**b**), is lost

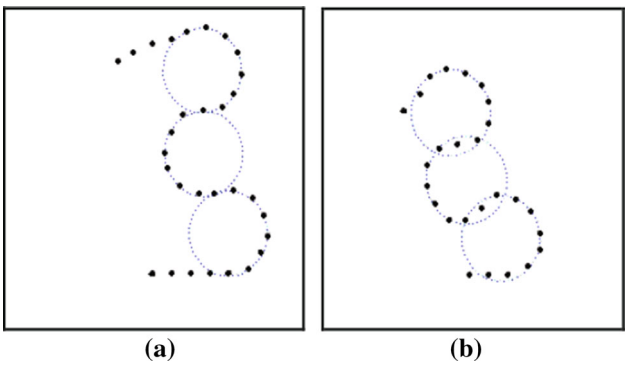

Fig. 9 Results of AGC processing of fragmented curve, illustrating enhancement. **a** is the original curve (i.e., the input to the system). **b** depicts the result of AGC processing of the curve shown in (**a**)

it "adapts" by the gain control, and there is no enhancement. The second example is comprised of a combination of straight lines and sectors of circles with opposing curvatures (Fig. 9). The AGC parameters used in this example of processing and "adaptation"/enhancement of curvature are $W(x) = k\frac{\gamma}{2}e^{-\gamma|x|}$; $k = 20$; $\gamma = 0.2$, with W extending across 5 pixels.

The first example illustrates curvature adaptation—the curvature is decreased, whereas the second highlights curvature enhancement (or emphasis). For presentation and comparison purposes, only, the curvature result of the second curve Fig. 9b is multiplied by a factor 1.87, to "compensate" for the adaptation effect and highlight the effect only on curvature enhancement. Blue circles have been added to Fig. 9 to highlight the changes in curvature at points of inflection. Points that are inside the circles have larger curvature than points that are on the circle. Therefore, the edge points (where a change in the curvature occurs) are emphasized similar to the edge enhancement depicted in Fig. 4a.

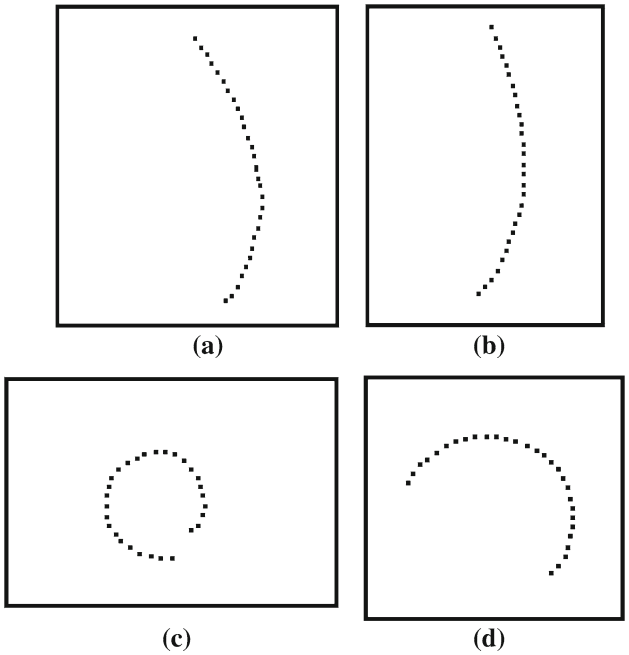

Fig. 10 Effect of noise and noise suppression demonstrated on a curve with constant curvature. **a** and **c** are curves with a constant curvature of 0.2 and 0.7, respectively, and additive positional Gaussian noise. **b** and **d** are the results of (**a**) and (**c**) processed by the AGC neural circuit, respectively. The noise suppression, characteristic of this processing, increases with the magnitude (i.e., the curvature) of the input

3.3.2 Curvature noise

As was highlighted in Sect. 2.4, one of the important features inherent in the processing of sensory data by AGC neural networks is the improvement of the SNR. This advantage of processing by AGC circuitry manifests itself along any dimension of the sensory signal, including structural dimensions such as curvature. Figures 10 and 11 demonstrate the effect of structural noise and noise suppression along the curvature dimension.

Comparing the noisy curves' traces with their traces after curvature AGC processing reveals noise suppression that monotonically increases with the magnitude. This is consistent with the SNR analysis of Sect. 2.4. Note that the noise is suppressed over the curved segments, whereas it is not affected at segments of zero curvature (i.e., the input value has magnitude of zero) (Fig. 11).

3.3.3 Size processing

To highlight the effect of AGC on size processing, we reconstruct the Ebbinghaus illusion experiment (Roberts et al. 2005), simulating the perceived target size by the AGC algorithm. In this case, we use a two-dimensional AGC model, as described at Sect. 3.1.4. For the sake of simplicity, each point consists of two spatial coordinates and a size value $\sigma(x, y)$.

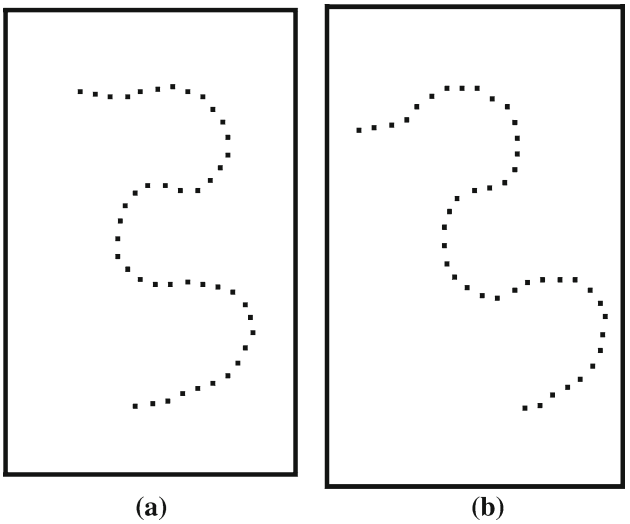

Fig. 11 Noise suppression demonstrated on noisy fragmented curve. A noisy fragmented curve, with curvature alternating between negative, −0.8, and positive, 0.8, is depicted in (**a**). Structural Gaussian noise is added to the curve. The result of processing the noisy curve by AGC neural network is shown in (**b**). Note that the noise is suppressed along the curved segments and not along segments of zero curvature

The generic input to the AGC operator, s(x), assumes in this case the form of a size map, which is used as the input of the AGC operator. The generic output, $r(x, y)$, which becomes now $\sigma_0(x, y)$, is a modified size map. Spatial correspondence between the input and output is maintained in this case. It is important to note that, again, for the sake of simplicity, each object is represented as a point at its center, with value of the object's size. We used to following AGC parameters: $W(r) = k\left(\frac{2}{121} - \gamma|r|\right)$, where $k = 5$, $\gamma = 0.00007$ and $r = \sqrt{x^2 + y^2}$. These parameters correspond to a lateral effect of a triangular W function with width of 121 image elements (pixels).

To illustrate the AGC effects on size processing, a setup of the psychophysical experiment was reproduced. Target was surrounded by 8 inducers at different radii (varying from 5 to 20 pixels). This was checked for near, medium and far (30, 40 and 50 pixels away from target, respectively) inducers. Target radius was 10 pixels. "Perceived" target size (in pixels) is shown in Fig. 12a as a function of inducer radius and distance. The AGC-processed results are consistent with the original experimental results. It is clear why increasing the inducer size decreases the target perceived size—this represents the size contrast effect of the AGC. It is less obvious why farther positioned inducers have stronger effect on target perceived size, than that of the closer inducers (i.e., decreasing the target size more effectively). The latter can be understood in the context of the AGC model by considering the effect of the mutual relation between the inducers on the effective (functional) width of W. According to the model of AGC visual processing, the impact of cells on their neighbors is limited by W. If the distance between cells is larger compared with W's effective width, then those cells will have a minimum effect on each other (if any). When an inducer is at a given distance x from the target, its distance from the other inducers varies from 0 to $2x$. Thus, when distance increases, more and more inducers are beyond the "influence zone" of the other inducers. This causes the perceived size of each inducer to

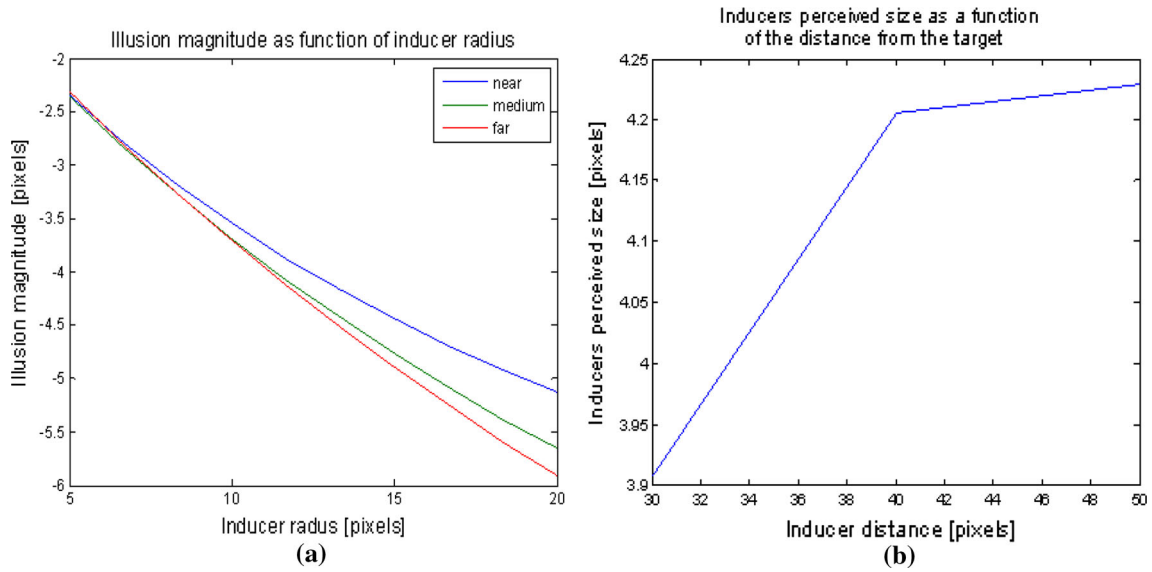

Fig. 12 **a** Results of reproduction of Ebbinghaus experiment by processing with feedback AGC. Varying the relative size and distance of the inducers produces changes in the apparent size of the target, consistent with the original experimental results. **b** Results indicating that inducers' perceived size is increased at larger distances. See text for more details

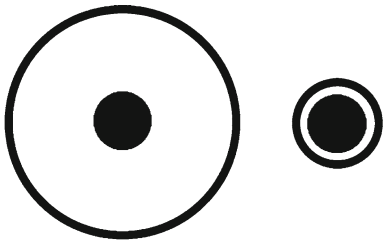

Fig. 13 Delboeuf illusion. The *dark disk* on the *right* is perceived larger than the one on the *left*, although they are of the same size

increase when the distance is increased. Figure 12b shows this phenomenon. Since the target is still inside the "influence zone" of the inducers, and the size of the inducers is now larger, the target seems smaller (the size-contrast effect is enhanced).

Note that here we considered only the target and inducers as objects with size. But, it is also possible that the visual system treats the space between the target and the inducers as an object with size. In this case, if the space between the target and the inducer is large, the inducer size has only a secondary effect, and the target size is determined mainly by the nearest object (e.g., see Fig. 13—Delboeuf illusion. In this illusion, the target gets smaller when the inducer diameter increases.). This model can explain also the moon size illusion, as well as other illusions. This example of size processing and the resultant nonlinear effects of the AGC on perceived illusion demonstrates the "programmable" characteristics of the AGC networks with feedback, wherein the effective network distance of cell influence is a function of both hardwired W and input structure.

3.3.4 Depth processing

To demonstrate the effects of feedback AGC on depth processing, we reproduce the experiment of Graham and Rogers's (1982), implementing the visual AGC neural network along the visual dimension of depth with the following spatial interaction parameters $W(x) = k\frac{\gamma}{2}e^{-\gamma|x|}$; $k = 1$; $\gamma = 0.2$, where the spatial interactions extend across 11 elements.

A depth-processing/perception scenario is as follows. Consider a three-dimensional scene shown for example on the upper-left corner of Fig. 14. The observation point is defined to be at the spatial coordinate of the center of the scene, with normalized height of 50 pixels.

For each point of the 3D original scene, the depth is calculated relative to the observation point. Figure 14 depicts the results in both 3D and cross sections. As a result of the processing by means of AGC, the left bar, **A**, which is at the same depth as the right bar, **B**, is now perceived closer to the observation point.

3.3.5 Convex–Concave (2D curvature processing)

Curvature can be defined in the three-dimensional case, i.e., on a surface. In this case, it characterizes the convexity/concavity of the surface structure. Curvature contrast adjustment is then executed by the AGC in a similar manner to its adjustment of the planner curvature. But, in this case the curvature information is embedded in a higher-dimensional space of $(x, y, z, \kappa_x, \kappa_y)$. We examine a simpler example that can be illustrated graphically in a simple manner. In this example, we assume that the characteristic curvature is separable into its κ_x and κ_y and consider its orthogonal components as one-dimensional curvatures. We can then use the one-dimensional algorithm described above. Figure 15 depicts the results in both 3D and cross section views of AGC convex–concave processing of a similar surface as at the depth-processing simulation above. As a result of the AGC processing (right column of Fig. 15), convexity and concavity are enhanced compared with the original input (left column of Fig. 15). Moreover, points that were originally at the same depth (as the left and right bars in the depth experiment above) are now perceived at different depths, consistent with depth-processing results.

4 Applications

Three applications of AGC-based image/visual processing are presented as examples. Two of them are along the intensity dimension, and the third is along the curvature dimension. Note that these are not the only possibilities and should be only regarded as examples.

4.1 High dynamic range images

High dynamic range (HDR) images are characterized by a very wide intensity range that exceeds by far the range that can be displayed on conventional displays. Examples for such images can be a scene combining indoor and outdoor details or scenes combining very bright spots and shadows. HDR images are obtained either by advanced digital imaging systems, or synthetically by algorithms that combine several images (see Zeevi et al. 1995; Debevec and Malik 2008 for such examples).

The common approach to dealing with this problem is to compress the intensity to a narrower range of display intensities (e.g., from approximately 16 bits down to less than 8 bits). Many algorithms have been presented in the literature for this purpose and can be divided into two main categories: tone-reproduction curves (TRC) and tone-reproduction-based operators (TRO). See Herscovitz and Yadid-Pecht (2004) for a summary.

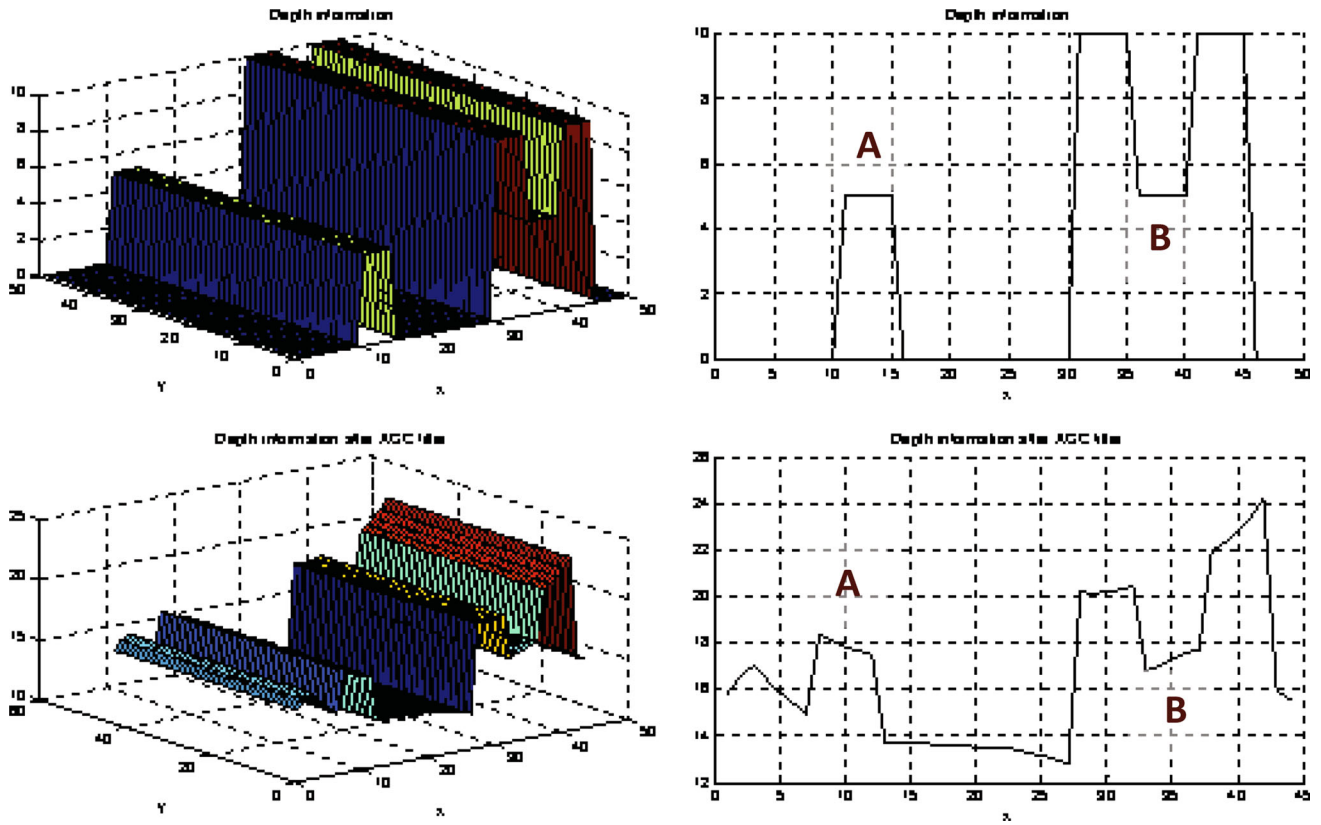

Fig. 14 AGC processing of depth information. Input and output of visual signals are displayed in the *top* and *bottom rows*, respectively. The *left column* is a 3D view, whereas the *right column* is a cross section view. Examining the *right column*, the *left bar*, **A**, is "perceived" as lying above the *right bar*, **B** (*lower right figure*), although they are physically at the same depth (*upper right figure*). This AGC-processed result is consistent with that of the original depth experiment

It is important to observe that such a task is executed easily by our visual system. Natural scenes span HDR of intensities, while the neural coding bandwidth is similar to that of a display or even narrower (approximately 6 bits Brajovic 2004). For this reason, some methods such as Ginosar et al. (1992), Zeevi et al. (1995), Brajovic (2004), Tanaka and Ohnishi (1997) are inspired by the HVS and attempt to mimic its function in order to compress the HDR of an image projected onto the limited, or low, dynamic range (LDR) characteristic of the retina or image acquisition devices. The AGC model proved to have high correlation with experimental results regarding intensity, and, as discussed earlier, one of its major characteristics is the compression of a wide dynamic rage. Therefore, it is natural to use AGC processing to compress HDR input into a narrower range, that can be displayed on a regular screen, and yet have a high sensitivity.

An LDR image (I_{LDR}) is obtained by adding a logarithmic version of the original HDR image (I_{HDR}), multiplied by attenuation constant (γ) to the response of the AGC model with I_{HDR} as the input (I_{AGC}). The logarithmic term adds some flexibility to the contribution of the ambient illumination:

$$I_{\mathrm{LDR}} = I_{\mathrm{AGC}} + \gamma \log(1 + I_{\mathrm{HDR}}), \tag{29}$$

where $\gamma = 0.004$ and $W = [0.4, 5, 0.4]$.

Using AGC has many advantages: Processing can be made in parallel over the entire image (especially when the AGC is implemented using ANN), just as it is implemented in the biological visual system, no "halo" artifacts appear, the relative contrast is increased (the AGC compresses the "common" attributes of the stimuli while enhancing the novelty) and, in general, the human observer that looks at this image on the screen gets an image that appears to look more "natural"—an image that is processed with a mechanism similar to the HVS and further enhances the natural processing. The important issue regarding the compression process is to preserve details in bright areas as well as details in the dark areas, together with the general illumination perception. This process is demonstrated by using a synthetic image (Fig. 16) and the Stanford Memorial Church HDR image (Fig. 17; taken from Paul Debevec's home page).

These results demonstrate that the system that mimics the biological visual system (i.e., its AGC feedback neural model) performs effectively in compressing HDR image into

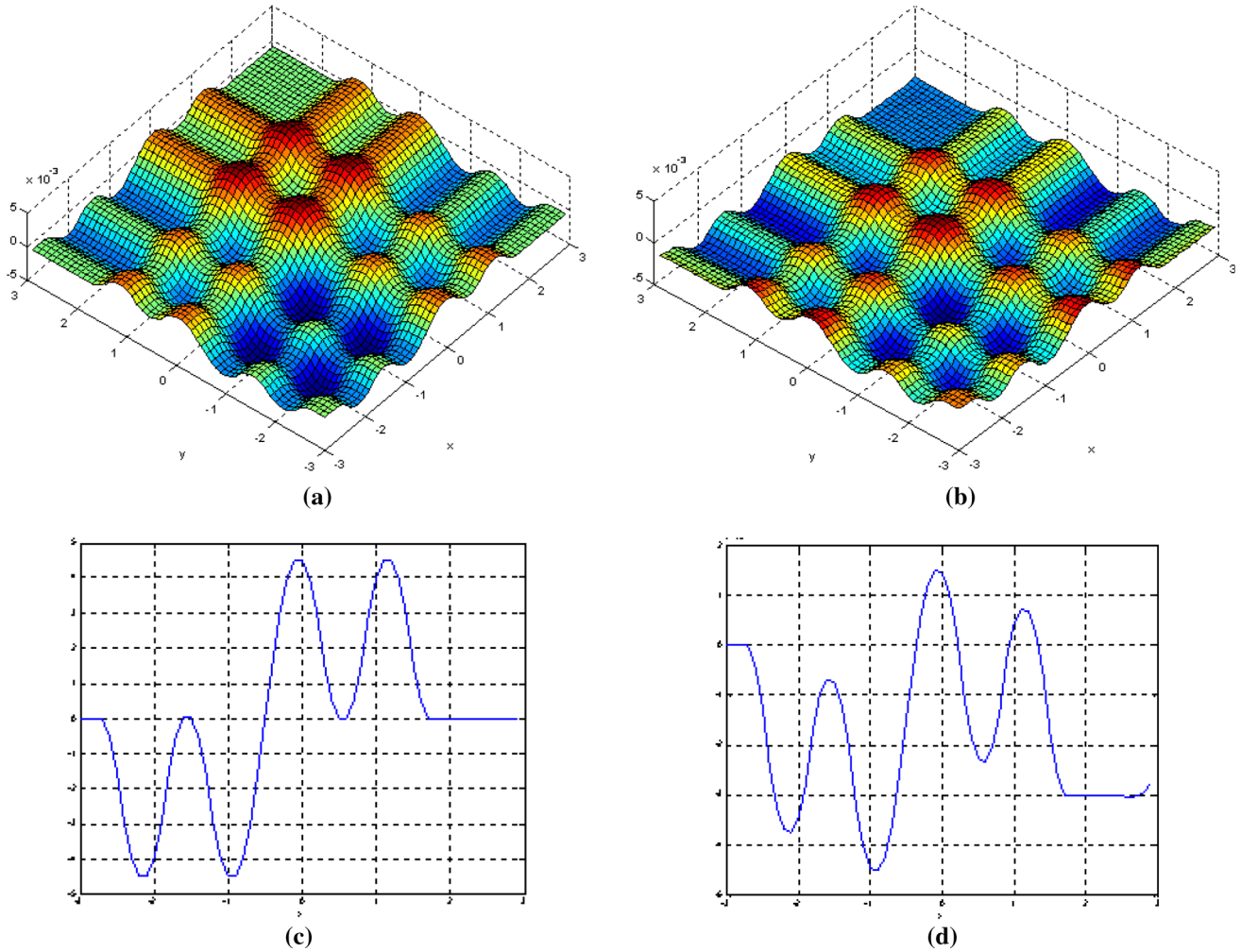

Fig. 15 AGC processing of convexity/concavity information. Shown are the visual signal input (**a**) and the response (**b**). Convexity and concavity are enhanced, as can be clearly seen in the cross section views (**c**) and (**d**) along the diagonal of the input and response, respectively. Moreover, examining the *right column*, the *left bar* is perceived as lying above the *right bar*, whereas they are physically at the same depth (*left column*). This is consistent with psychophysical depth-processing results (see Fig. 14 for comparison)

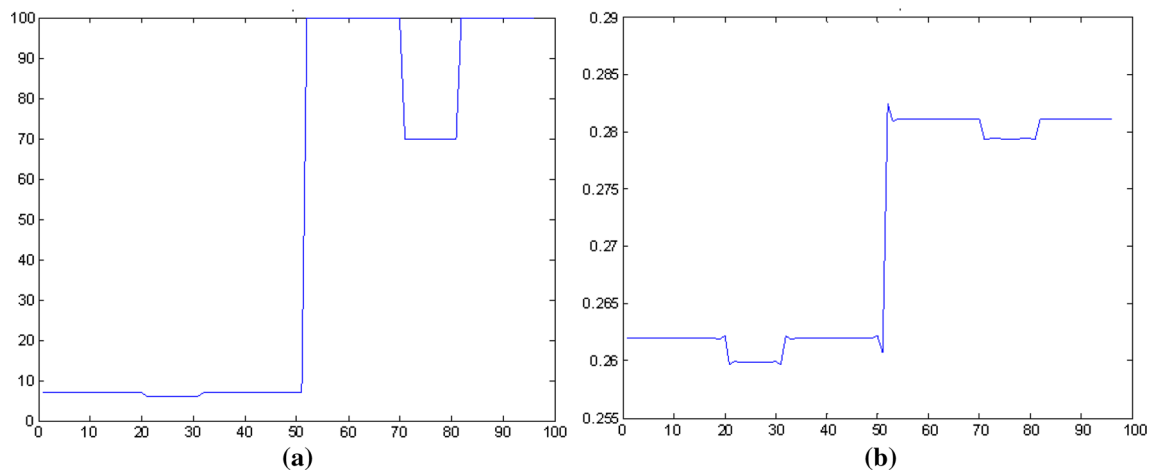

Fig. 16 **a** Simple example of HDR image combining two illumination regions and details in both of them. **b** The result of the processing by the feedback AGC. The dynamic range is compressed, while both details and illumination perception are preserved

(a) **(b)**

Fig. 17 The Stanford Memorial Church LDR image obtained by using **a** MATLAB function "tonemap," **b** feedback AGC. This technique is completely free of halo artifacts, contrary to the MATLAB function (see the dark region *marked in arrow* in (**a**). Even though some regions of (**b**) seem darker than those of (**a**), the result obtained by application of the method presented herein is more realistic, yielding more similar image to what we expect to see when observing such a scene

LDR image as required by most conventional displays. An important feature characteristic of the AGC-based processing approach is that local details are well preserved and in some cases are even enhanced. Comparing the performance of processing with AGC, with the default MATLAB function shows that the AGC-based processing performs at least equally well, and in some cases even better. A very important property of processing by the biological-based AGC is that it is completely free of halo artifacts, contrary to the MATLAB function (see the dark region in Fig. 17a). Moreover, the result obtained by application of the biologically motivated method is more realistic, yielding results more similar to what we expect to see when observing such scene.

4.2 Enhanced edge detection

An important problem in image processing is the detection of edges in a given image. A number of schemes have been proposed for this purpose (Peli and Malah 1982). These are applied as a preprocessing operation prior to high-level image analysis. Edge detection is assumed to be a crucial step in the visual path, and part of the early visual processing (Marr and Hildreth 1980).

Canny's edge detector (Canny 1986) is still considered to be a good and standard benchmark of edge detection for many purposes. It is based on first-order operators (discrete derivative), which produce an output that corresponds to the difference between the values of neighboring pixels. Such operators cannot, however, consistently locate object boundaries in the presence of changes in scene illumination, and second-order operators cannot resolve this problem (Johnson 1990).

An example of such a case is highlighted in Fig. 18. To overcome this limitation, we can extract the edges of an image by preprocessing with AGC. As discussed earlier, by processing an image with AGC, we get a local spatial adaptation, which diminishes the slowly varying of illumination over the global scene. In addition, processing by HVS-based AGC also enhances sharp variations, thus increasing the relative contrast or slope of edges, while suppressing the noise, similar to the HVS, which extracts edges much better than Canny edge detector. Therefore, applying AGC processing prior to the application of first-order edge detection (such as canny's) is expected to enhance the performance of edge detection over poorly illuminated environments.

4.3 Curve completion due to occlusion

Contour interpolation, in painting the missing parts between two contour fragments, is a ubiquitous phenomenon. Numerous objects that appear in natural images are bounded by edges that are not fully defined by visual information. In many cases, this visual information deficiency stems from partial occlusion by surrounding objects; in other cases, incomplete edge specification arises from a lack of contrast with the background environment. Contour interpolation in vision leads to the perception of clearly defined object boundaries even though these boundaries are missing [see Fig. 19 for examples of this phenomenon].

A brief review on this subject can be found in Ben-Yosef and Ben-Shahar (2010), where the authors concluded that

Fig. 18 Example of edge extraction in regions with poor illumination. **a** An image with regions of poor illumination marked by *red ellipses*. **b** Edges obtained by applying Canny operator. Edges at the marked regions are not detected due to poor illumination. **c** Edges enhanced by the application of the Canny edge detector to the image preprocessed by the AGC operator. Edges at the marked regions are now detected (color figure online)

Fig. 19 Examples of curve completion due to **a** lack of contrast with the background [adopted from Ben-Yosef and Ben-Shahar (2010)]. **b** Partial occlusion [adopted from Kimia et al. (2003)]

curve completion is an early visual process that takes place as low as at the primary visual cortex, and that the participation of early visual neurons in the representation of curves is not limited to viewable curves only, but is also extended to completed or illusory curves as well (see also Guttman and Kellman 2004). These findings and ideas suggest that contour interpolation involves basic neural mechanism and that real and interpolated contours are processed in parallel. Therefore, it may be concluded that network-type models of completion processes are most likely to be the mechanism underlying contour interpolation.

Indeed, many networks for curve completion have been introduced in the literature (e.g., Yen and Finkel 1998; Field et al. 1993). But, although Singh and Fulvio (2005) concluded that the visual system systematically takes into account the curvature of inducing contours when extrapolating their shapes and that a successful model must take into account the curvatures, all of them use array of cells selective for orientation.

Kimia et al. (2003), motivated by railroad design methods of the early 1900s which connects two rail segments by "transition curves," proposed the minimization of an energy functional that penalizes changes in curvature as a completion model, i.e., minimizing the following:

$$\int \left(\frac{d\kappa}{ds}\right)^2 ds. \tag{30}$$

This kind of minimization immediately entails a linear expression for the curvature as a function of the arc length, a class of curves known as Euler spirals. Although this model satisfies all the axioms mentioned in Ben-Yosef and Ben-Shahar (2010), it fails to predict some experimental results (Singh and Fulvio 2005), since the interpolated curvature should decrease asymptotically to zero if no end segment exists (i.e., the curve is extrapolated from only one segment), and a nonlinear decrease in the curvature fits better the results than a linear decrease.

Based on the above insights, and motivated by our model of the HVS, we propose a novel model for curve completion that combines both the AGC and the Euler spirals in a network-style model. The idea is that the curve completion is performed along the curvature dimension. The missing curvature data of the curve are linearly interpolated between the curvature value of the first segment to the curvature value of the second segment. The interpolated curve is then entered as an input to the AGC network. The response of the system is the perceived curve. If only one segment exists, the second segment is referred to as a zero curvature segment. In this way, the extrapolated curve has a nonlinear decrease in its curvature as suggested above. Moreover, this model can explain the "cost of curvature" (Singh and Fulvio 2005), and scale dependency (Fantoni and Gerbino 2003; Gerbino and Fantoni 2006), of the interpolated curves.

The "cost of curvature" means that the precision with which an interpolated contour is represented becomes sys-

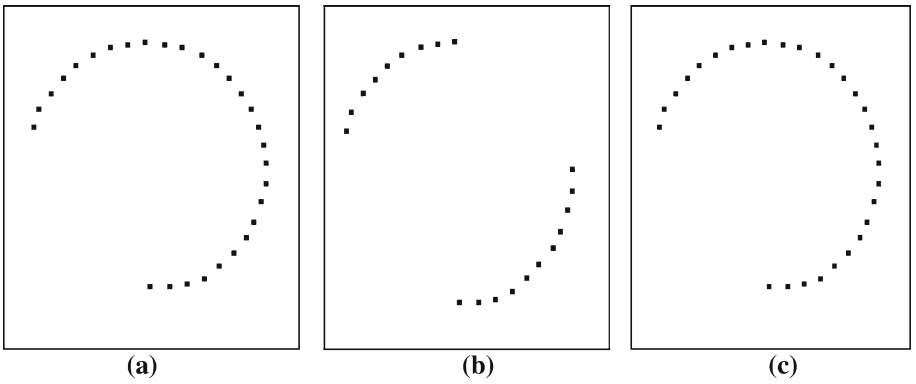

Fig. 20 Simulation result for interpolating a curve with a constant curvature. **a** Original curve. **b** The occluded curve. **c** The interpolated curve. The occluded segment is a linear combination of the contour fragments and, thus, (**c**) is identical to (**a**)

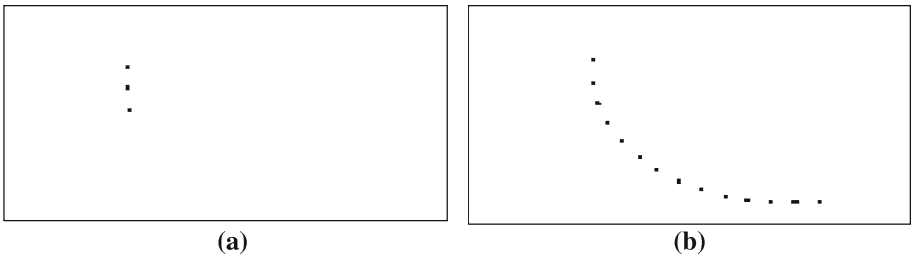

Fig. 21 Simulation result of extrapolating a curve, given a short segment. **a** The given segment. **b** The extrapolated curve

tematically weaker with increasing curvature. This is interpreted in the context of the AGC model according to the small signal analysis as follows: When the input intensity is higher (e.g., the curvature increases), the sensitivity of the system decreases.

Scale dependency means that the interpolation depends on the viewing distance. This is an obvious outcome for interpolating the curve along the curvature dimension. The curvature depends on the curve radius, and the radius, in turn, is a function of the viewing distance.

The model is tested on a few simple curves to demonstrate the main ideas. For each curve, an occlusion is simulated by removing part of the curvature information. The missing curvature values are then linearly interpolated between the last curvature value of the first segment to the first curvature value of the second segment. The interpolated curvature values serve as input to the AGC model, and the response is referred to as the interpolated curve. The parameters of the AGC are $W(x) = 1\,[\text{length of W}]$, with W extending across 11 pixels. Figure 20 depicts the result of completion of a curve with constant curvature (i.e., segment of a circle). As this example may look very simple and of no value, one should keep in mind that this result is simple only because the curve is interpolated along the curvature dimension. If, for example, the curve would have been interpolated along the tangent dimension, the problem would become more complicated. Figure 21 depicts the result of curve completion for the case when only one segment is present. Note how the curvature values decrease to zero (as noted in Singh and Fulvio 2005). Figure 22 depicts curve completion when a sudden and abrupt change in curvature occurs. Part of the curve consists of some constant curvature value, while the other part consists of the same constant curvature but of opposite sign. When the occluded portion increases in length, the interpolated curve becomes smoother, and the changes compared with the original curve become much more noticeable. Nevertheless, one should keep in mind that the interpolated curve should not be compared with the original curve, but with the curve that a human observer will perceive. Figure 22e is consistent with what a human observer would draw based on the given occluded curve (d).

5 Discussion and conclusions

Biological and man-made visual systems, alike, are concerned with detection and enhancement of novelty associated with visual scenes. Novelty is associated with the unexpected that cannot, for example, be linearly predicted. Qualitatively speaking, important and interesting "events" along image contours, for example, consist primarily of abrupt changes in orientation and curvature, as is the case with other image attributes (dimensions). Local maxima of curvature, and inflection points (i.e., zero crossings of curvature) identify in this case such events (see Hoffman and Richards 1984; Koenderink and Doorn 1982; Richards et al. 1986; Fischler and Bolles 1986). This fact is well known by artists and cartoonists who exploit it in their artwork, as much as they do, and in more familiar manner, with regard to other image attributes such as intensity and color. Moreover, zero crossings along curvatures (i.e., points of inflection) can constitute the basis of shape representation for planar curves (Mokhtar-

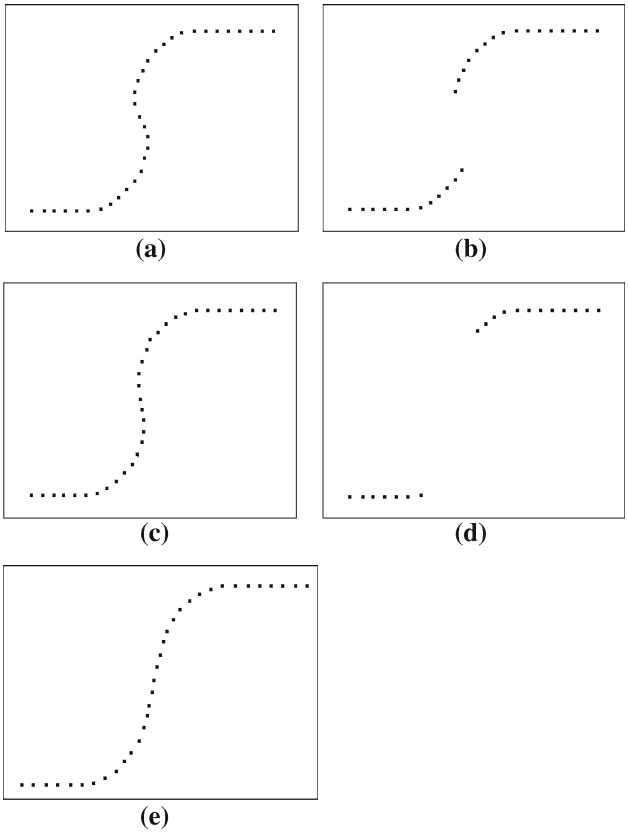

Fig. 22 Simulation result for interpolating curve with an abrupt change in curvature. **a** Original curve. **b** The occluded curve. **c** The interpolated curve. **d** A curve with a longer occluded region. **e** The interpolated curve. The occluded part is where the abrupt change in curvature occurs and thus (**c**) and (**e**) are only a smooth version of (**a**). The occluded part in (**b**) is small, and therefore, the changes in (**c**) are almost unnoticeable. The occluded part in (**d**) is large, and therefore, the changes between (**a**) and (**e**) are quite significant but, nevertheless, **e** is a continuous curve

ian and Mackworth 1992). Similar to biological visual systems that emphasize changes and adapt to locally constant values of the image attributes, this is indeed an important feature of curvature processing (or of processing of other image attributes) by adaptive computer vision and image-processing systems endowed with the mechanism/algorithm of AGC. Curvature emphasis and adaptation (see Figs. 8, 9) occur simultaneously, and their extent can be controlled by adjusting the parameter κ of the "hardwired" connectivity.

Inspection of the results of size processing indicates a good correspondence between the AGC system response (Fig. 12a) and the psychophysical experimental results (Fig. 6), for both the distance and size parameters. Such results are expected in view of the dependency of AGC on these two parameters as well, i.e., cells proximity and specificity (in this case, objects' size).

Inspecting the results of depth processing indicates a good correspondence between the AGC system response (Fig. 14) and the psychophysical experimental results (Fig. 7). Moreover, these results can be understood also from the convex/concave AGC viewpoint (Fig. 15). This leads to the conclusion that depth sensitivity adjustment may be understood also in relation to curvature adjustment by gain control (and, perhaps gain control along other visual dimensions) or vice versa.

Understanding the HVS and modeling some of its characteristics by a generic sensory mechanism of AGC is of considerable interest because of its potential implementation in the design of intelligent computer vision and image acquisition and processing algorithms and systems. Because of the complexity of the processes involved, and in order to account for the vast amount of available experimental data, there is a need for relatively simple generic models. As shown, the generalized AGC system is relatively simple (only few parameters) and versatile. It does not call for postulating any components of neural circuitry more complex than those well known to exist in biological neural networks and, yet, shows good correlation with psychophysical experiments. Such understanding has become crucial in view of the fact that visual prosthetics are becoming a workable reality. These visual prosthetics use a variety of biomedical and technological approaches such as stimulating the visual cortex or even the retina (Tran et al. 2009; Dobelle 2000). In all these studies, the subjects have to be trained for recognizing and discriminating different patterns of simulations (Humayun 2003). The main concern of these studies is whether the subject can recover/develop a visual perception and what are the proper stimulus parameters. Only a few of these studies has considered, however, the important question of what are the optimal stimuli, i.e., how should the computing elements (neurons) be stimulated in order to achieve the best visual perception of a given image [see, e.g., the optimization procedure proposed by Liu et al. (2009)]. Such visual stimulation may be based on our understanding of fundamental visual mechanisms such as those presented, for example, in this study.

Implementing the AGC mechanism in the context of all image elementary attributes (dimensions), or other modalities for this matter, yields great advantages. It constitutes a universal and parsimonious model that explains how our visual system processes visual information along its various dimensions, before the later stage of sequential "visual routines" is implemented. Such a mechanism can process an image along all its dimensions (that are yet to be explored). The only necessary information is the relevant projections. Further, it may lead to the development of a metric for distance between images, and it can be instrumental in performing important tasks, such as recognition and classification. Such computer vision tasks can be executed along the different feature dimensions and be further mapped nonlinearly without recombination of the separate processed feature maps back onto an image. Alternatively, the AGC mechanism

can be applied on a surface or manifold representation of the visual (image) data, embedded in a higher-dimensional-combined position-and-features' space or Riemannian manifolds. An important property of this embedding is that such Riemannian manifolds are endowed with a bilinear positive-definite symmetric tensor which constitutes a natural metric (Kimmel 2003; Kimmel et al. 2000; Sochen and Zeevi 1998). To get an intuitive glimpse into the essence of image embedding, a gray-level image (visual) representation is considered to be a two-dimensional Riemannian surface embedded in a three-dimensional manifold, whereas a colored image is embedded in a five-dimensional spatial-feature manifold or, for the sake of simplicity (avoiding the generalization of the proper norm for gradients), the embedding of a colored image is in a five-dimensional Euclidean spatial (i.e., position)-feature space. Likewise, additional features (i.e., image attributes or image dimensions), such as curvature, size, orientation and more, increase the dimension of representation space. The AGC processing then manifests itself in the evolution of the image manifold. Whereas the details (and/or implementation) of this approach are beyond the scope of the present study, it is important to note that curvature of such surfaces and manifolds becomes central to this approach of representation of visual and other modalities of sensory information, as the curvature replaces the well-known and widely used Shanon-Nyquist criterion of "bandwidth" (which is not yet fully understood in the context of feature dimensions, rather than spatial dimesnions) (Saucan et al. 2008). As much as this topic is fundamental to the understanding of neurobiological and computer vision representations and to processing of sensory data, it is also beyond the scope of this paper. [The reader is referred to Saucan et al. (2008) and additional papers by the same authors for further detailed exposition of the topic of curvatures and bandwidth.]

The AGC model elucidates the ability of our HVS to span HDR of inputs along various dimensions, while still having high sensitivity. This ability has been well known and investigated with reference to the intensity dimension. Here, we have shown how powerful it can be along other dimensions. For example, we have highlighted how we can be sensitive to curvature values that vary over a wide range (the limit is defined only by the retina resolution), and yet notice differences between curves in the order of 10^{-5} (Watt and Andrews 1982; Watt 1984 for more details). This interpretation is valid also for depth perception (see Kaye et al. 1999; Kumar and Glaser 1992 for more details), size, texture, orientation, motion and more.

It appears as though the AGC mechanism repeats itself along all stages of sensory processing in the CNS (Abbott et al. 1997; Salinas 2000; Sit et al. 2009), in order to remove redundancy (Schwartz and Simoncelli 2001). Therefore, this model allows us to mimic the HVS (or other sensory modalities), in biologically motivated man-made intelligent sensory systems, and to propose a unified model for biological sensory processing.

Likewise, feedback AGC model allows also to process an image not only in the intensity/spatiotemporal domain, but also along all other visually important (or other sensory) dimensions. For example, in the case of a given noisy curve, one can further reduce the noise along the curvature dimension (in addition to the AGC-based noise reduction) with standard filters, such as a nonlinear diffusion filter. As discussed above, one can also overcome occlusions by interpolating along the curvature dimension and create HDR images, or enhance edge detection processing along the intensity dimension.

The proposed visual AGC mechanism can enhance existing schemes of intelligent image processing with reference to enhancement of various image attributes and features, i.e., curvature, size and other image attributes.

The projection and decomposition of an image into its intrinsic dimensions is by no means the only possible model of representation and processing of images, and definitely not always the optimal one. Inferring from what is known about retinal (foveal) projection onto the visual cortex, in this work we considered the projections and AGC-based processing of various image attributes independently of each other. The assumption of independency shoud, however, be further investigated and the alternative approach of image representation as two-dimensional manifolds, embedded in a higher dimensional Euclidean space or Riemannian manifold, should be studied in detail. This, of course entails theoretical and computational challenges, but it is likely to result in new ideas in theoretical neurobiology and brain sciences. Likewise, as far as computer vision is concerned, the AGC-based processing of image manifolds embedded in higher-dimensional-combined spatial-feature spaces or Riemannian manifolds is likely to enhance visual saliency and cognitive attributes.

Appendix 1: Uniqueness of the AGC solution

We prove (based on Shefer 1979) that if a solution of the AGC model exists, it is unique, assuming $s(x) > 0$. In fact, it is sufficient to prove uniqueness for the feedback signal, $f(x)$, derived from (3) and (4):

$$f(x) = \int s(x') \left[\alpha - f(x')\right] W(x - x') dx'. \tag{31}$$

We prove that if two bounded solutions of (31) exist, $f_1(x)$ and $f_2(x)$, they must be identical. To this end, we define the difference between the two assumed-to-exist solutions:

$$b(x) \underline{\underline{\Delta}} f_2(x) - f_1(x). \tag{32}$$

$f_1(x)$ and $f_2(x)$ are bounded, and therefore, $b(x)$ is also bounded. We define its maximum value:

$$M_b \underset{=}{\Delta} \max_x |b(x)| . \tag{33}$$

Substituting Eq. (31) in Eq. (32) we get:

$$\begin{aligned} b(x) &= \int s(x') \left[\alpha - f_2(x')\right] W(x - x')dx' \\ &\quad - \int s(x') \left[\alpha - f_1(x')\right] W(x - x')dx' \\ &= \int s(x') \left[-f_2(x') + f_1(x')\right] W(x - x')dx' \\ &= -\int s(x')b(x')W(x - x')dx'. \end{aligned} \tag{34}$$

Assuming that $s(x)$ is bounded, we define its maximum value:

$$M_s \underset{=}{\Delta} \max_x |s(x)| . \tag{35}$$

From all the above we get:

$$\begin{aligned} M_b &= \max_x \left| \int s(x')b(x')W(x - x')dx' \right| \\ &\le \max_x \int \left|s(x')\right| \left|b(x')\right| \left|W(x - x')\right| dx'. \end{aligned} \tag{36}$$

Substituting Eqs. (33) and (35) in Eq. (36) we get:

$$\begin{aligned} M_b &\le \max_x \int M_s M_b \left|W(x - x')\right| dx' \\ &= M_s M_b \max_x \int \left|W(x - x')\right| dx'. \end{aligned} \tag{37}$$

Substituting Eq. (6) in Eq. (37) we get:

$$M_b \le M_s M_b \max_x S_W = M_s M_b S_W \tag{38}$$

and thus

$$M_b \le M_s M_b S_W. \tag{39}$$

For $M_s S_W < 1$, Eq. (39) is valid only if $M_b = 0$, which implies that there is a unique solution for Eq. (31).

The meaning of $M_s S_W < 1$ is the condition for unique solution given $s(x) \ge 0 \; \forall x$ given in (35), i.e., $\max_x\{s(x)\} < 1/S_W$.

If the assumption of $s(x) > 0$ is not valid, and $s(x)$ assumes also negative values (as is the case for curvature values), the above proof is still valid, by taking the absolute value of the feedback: $f(x) \to |f(x)|$, in which case Eq. (31) becomes

$$f(x) = \int s(x') \left[\alpha - \left|f(x')\right|\right] W(x - x')dx', \tag{40}$$

and the rest of the proof is unaffected.

Appendix 2: The curve-construction algorithm

The basic principle underlying drawing of a curve determined by its curvature information is based on Eq. (28) which approximates the curve by an arc of radius R (Fig. 23). This is a good approximation under the following assumptions.

Assumptions

Curvature, per definition, is a quadratic term. As such, the forward problem (calculating the curvature vector of a curve) is a well-posed problem and can be dealt with easily. On the other hand, the backward problem, which is drawing a curved line from its curvature information only, is an ill-posed problem, rendering it impossible to solve without making some assumptions. Further, the filtering process is a non-linear necessitating additional assumptions. These assumptions are:

1. The curved line is discrete.
2. The line is smooth enough.
3. The starting point of the line is known and is not affected by filtering.
4. The tangent to the curve at the first point of the curve is known and does not change by the filtering.
5. The length of the original curve between each sequential point is known and does not change by filtering. Therefore, curve length is constant.
6. Curvature information is known (or given).
7. Curvature values are positive for counter clockwise (CCW) curve and negative for clockwise (CW) curve as defined in Fig. 24.
8. Centered coordinates are implemented, i.e., the point (0, 0) coincides with the center of the image.

The algorithm

The algorithm is, as mentioned, based on approximating curve segments by circular segments. This is done by calculating for each point on the curve the center point of a circle that matches the point's curvature and position. Then, an arc (part of a circle) is drawn in the same length of the original curve segment. Figure 23 shows this idea and the algorithm variables.

Given the curvature vector, the starting point and its tangent orientation, and the arcs lengths, one can draw the curved line following these steps (see Fig. 25 for summary):

1. Calculate the correct center point

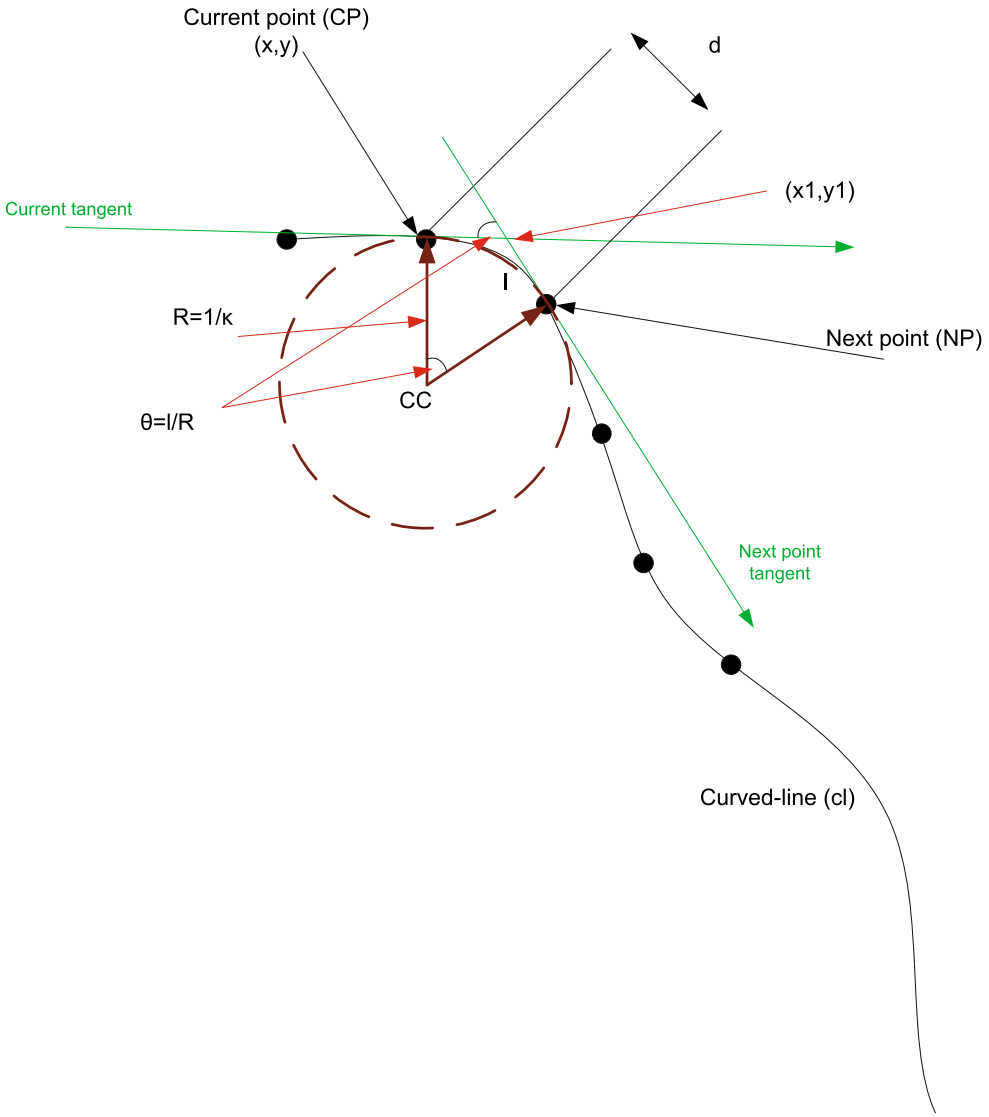

Fig. 23 Curve-construction tool: variables' definitions

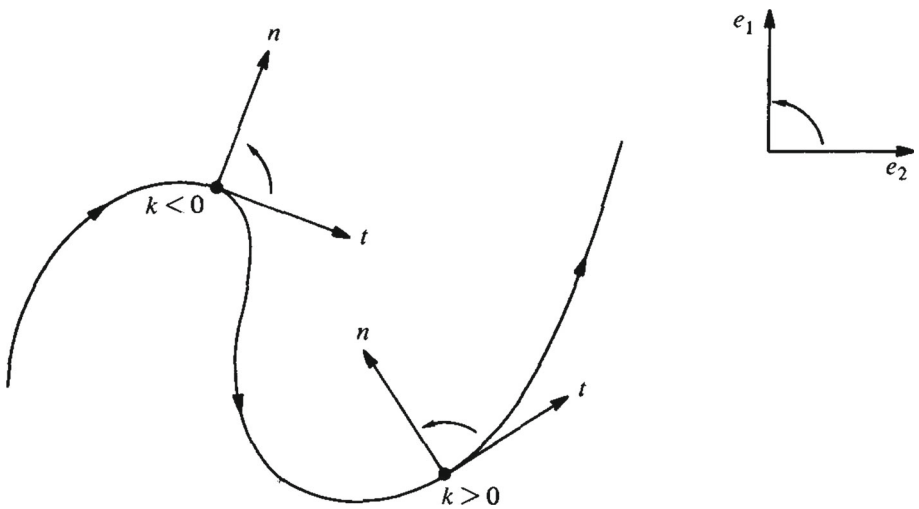

Fig. 24 Definition of signed curvature definition: The curvature is defined as positive if the unit tangent rotates counter clockwise, and negative if it rotates clockwise

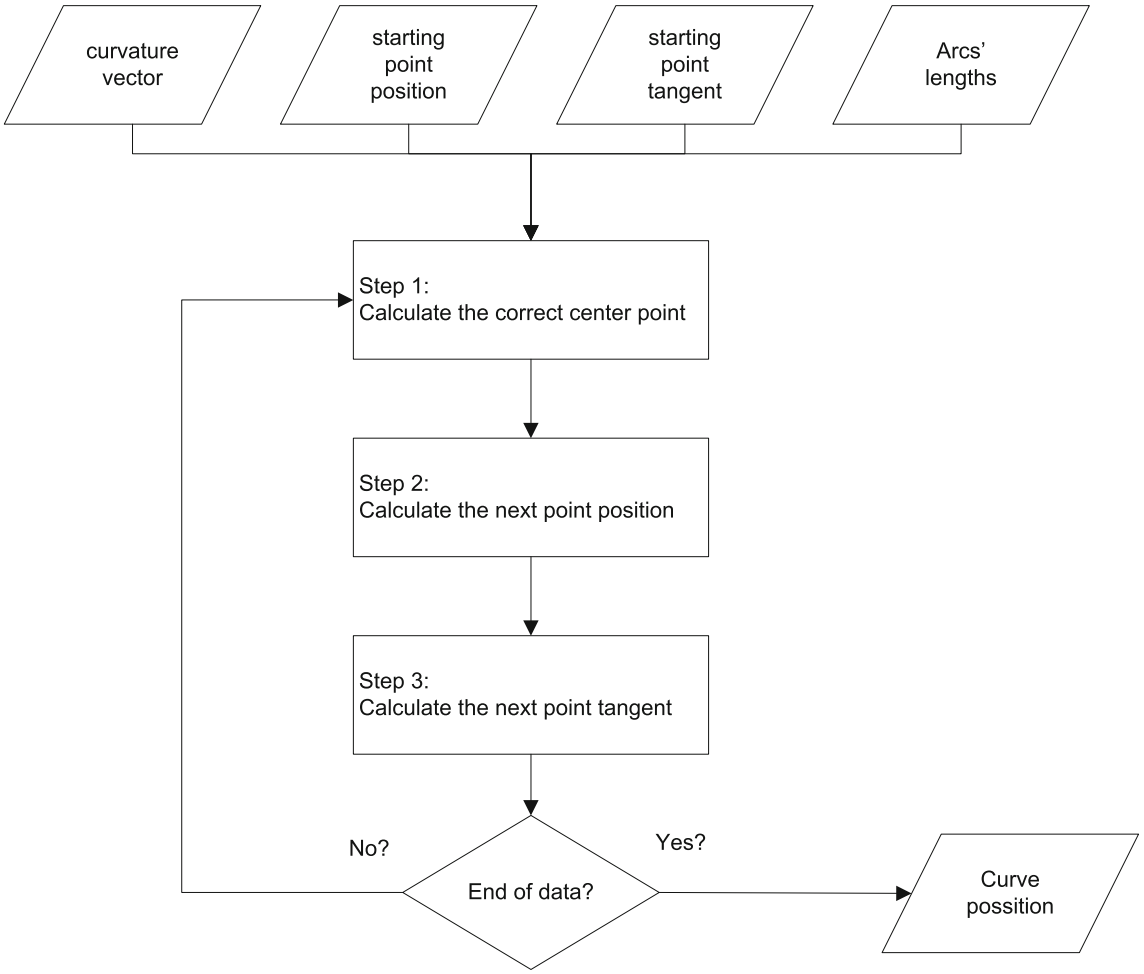

Fig. 25 A flowchart of the curvature drawing-tool algorithm

"CC" (see Fig. 23) is the center point of a circle that match the curvature at CP according to Eq. (28).
This point must satisfy two equations, as follows:

- Radius connecting CC and CP is perpendicular to the tangent at CP,

$$\overrightarrow{\mathrm{CC}-\mathrm{CP}}\cdot\overrightarrow{\mathrm{cl}'(\mathrm{CP})}=0, \tag{41}$$

  where $\mathrm{cl}'(\mathrm{CP})$ is the derivative of the curved line cl at CP.
- Curvature can be represented locally by a circle with radius length equal to $1/\kappa$:

$$(\mathrm{CC}_x-\mathrm{CP}_x)^2+(\mathrm{CC}_y-\mathrm{CP}_y)^2=(1/\kappa)^2=R^2 \tag{42}$$

  The above equations have two solutions for center points. One possible solution fits the positive curvature, and the other one fits the negative curvature. The correct point is thus chosen according to the curvature sign.

For negative curvatures (as the one in Fig. 23), the correct point is to the right of the tangent vector and to the left for positive curvatures.

2. Calculating the next-point position (NP) Calculate the next point according to an arc that has the following characteristic:
   - Starts from the current point. Has radius equal to $1/\kappa$.
   - Is an arc belonging to a circle with central point CC, calculated in the previous step.
   - Has the same length as the original segment. (This is equivalent to saying that to the arc corresponds an angle θ).
3. Calculating the next-point tangent
   - Calculate θ according to the following equation:

     $$\theta=l/R=l\cdot\kappa,$$

     where l is the length of the arc connecting CP and NP.

- Calculate the angular orientation of the current tangent.
- Calculate the orientation of the tangent at NP with reference to the one at CP:

$$\sphericalangle \mathrm{cl}'(\mathrm{NP}) = \sphericalangle \mathrm{cl}'(\mathrm{CP}) + \theta$$

- For (curvature < 0): $\sphericalangle \mathrm{cl}'(\mathrm{NP}) = \sphericalangle \mathrm{cl}'(\mathrm{CP}) - \theta$
- Calculate (X_1, Y_1) according to the point of intercept of the current tangent and the subsequent point tanget.
- Calculate the next-point tangent by subtracting (X_1, Y_1) from NP.

Note:

1. In case the curvature is equal to 0:
   - Next-point tangent is equal to current tangent.
   - Next point is calculated by taking the original segment length along the direction of current tangent.
2. Calculating (X_1, Y_1) is necessary (although the next-point slope is known) because of the fact that the slope orientation is not known (it is the output of an arctan function). As noted above, the orientation of the tangent is important in determining the correct CP.

References

Abbott LF, Varela JA, Sen K, Nelson SB (1997) Synaptic depression and cortical gain control. Science 275(5297):221–224

Ben-Yosef G, Ben-Shahar O (2010) Minimum length in the tangent bundle as a model for curve completion. In: Computer vision and pattern recognition, pp 2384–2391

Blakemore C, Campbell FW (1969) On the existence of neurones in the human visual system selectively sensitive to the orientation and size of retinal images. J Phys 203(1):237–260

Brajovic V (2004) Brightness perception, dynamic range and noise: a unifying model for adaptive image sensors. In: Computer vision and pattern recognition. Proceedings of 2004 IEEE computer society conference (2):II-189-II-196

Canny J (1986) A computational approach to edge detection. IEEE Trans Pattern Anal Mach Intell 8(6):679–698

Carey DP, Harvey M, Milner AD (1996) Visuomotor sensitivity for shape and orientation in a patient with visual form agnosia. Neuropsychologia 34(5):329–337

Cavanagh P, Arguin M, Treisman A (1990) Effect of surface medium on visual search for orientation and size features. J Exp Psychol Hum Percept Perform 16(3):479–491

Coltheart M (1971) Visual feature-analyzers and aftereffects of tilt and curvature. Psychol Rev 78(2):114–121

Curran W, Johnston A (1996) Three-dimensional curvature contrast-geometric or brightness illusion? Vis Res 36(22):3641–3653

Du Croz JJ, Rushton WAH (1966) The separation of cone mechanisms in dark adaptation. J Physiol 183(2):481–496

Debevec PE, Malik J (2008) Recovering high dynamic range radiance maps from photographs. In: ACM SIGGRAPH 2008 classes. Los Angeles, California, pp 1–10

Ding J, Sperling G (2006) A gain-control theory of binocular combination. Proc Nat Acad Sci USA 103(4):1141–1146

Do Carmo M (1976) Differential geometry of curves and surfaces. Prentice-Hall, Upper Saddle River

Dobbins A, Zucker SW, Cynader MS (1987) Endstopped neurons in the visual cortex as a substrate for calculating curvature. Nature 329:438–441

Dobelle WH (2000) Artificial vision for the blind by connecting a television camera to the visual cortex. ASAIO J 46(1):3–9

Enns JT, Rensink RA (1990) Influence of scene-based properties on visual search. Science (New York, NY) 247(4943):721–723

Enns JT, Rensink RA (1990) Sensitivity to three-dimensional orientation in visual search. Psychol Sci 1(5):323–326

Faisal AA, Selen LPJ, Wolpert DM (2008) Noise in the nervous system. Nat Rev Neurosci 9(4):292–303

Fantoni C, Gerbino W (2003) Contour interpolation by vector-field combination. J Vis 3(4):281–303

Farzin M, Suomela R (1998) Robust image corner detection through curvature scale space. IEEE Trans Pattern Anal Mach Intell 20(12):1376–1381

Field DJ, Hayes A, Hess RF (1993) Contour integration by the human visual system: evidence for a local 'association field'. Vis Res 33(2):173–193

Fischler MA, Bolles RC (1986) Perceptual organization and curve partitioning. IEEE Trans Pattern Anal Mach Intell 8(1):100–105

Furman GG (1965) Comparison of models for subtractive and shunting lateral-inhibition in receptor-neuron fields. Kybernetic 2(6):257–274

Gerbino W, Fantoni C (2006) Visual interpolation is not scale invariant. Vis Res 46(19):3142–3159

Gibson JH (1937) Adaptation with negative after-effect. Psychol Rev 44(3):222–244

Ginosar R, Hilsenrath O, Zeevi YY (1992) United States Patent: 5144442–Wide dynamic range camera, U.S. Patent 514444201

Graham M, Rogers BJ (1982) Simultaneous and successive contrast effects in the perception of depth from motion-parallax and stereoscopic information. Perception 11(3):247–262

Gregory RL (2009) Seeing through illusions. Oxford Univ. Press, New York

Griffin LD, Lillholm M, Nielsen M (2004) Natural image profiles are most likely to be step edges. Vis Res 44(4):407–421

Guttman SE, Kellman PJ (2004) Contour interpolation revealed by a dot localization paradigm. Vis Res 44(15):1799–1815

Hancock S, Peirce JW (2008) Selective mechanisms for simple contours revealed by compound adaptation. J Vis 8(7):1–10

Herscovitz M, Yadid-Pecht O (2004) A modified multi scale retinex algorithm with an improved global impressionof brightness for wide dynamic range pictures. Mach Vis Appl 15(4):220–228

Hochstein S, Ahissar M (2002) View from the top: hierarchies and reverse hierarchies in the visual system. Neuron 36(5):791–804

Hoffman DD, Richards WA (1984) Parts of recognition. Cognition 18(1–3):65–96

Hubel DH, Wiesel TN (1968) Receptive fields and functional architecture of monkey striate cortex. J Phys 195(1):215–243

Hubel DH, Wiesel TN (1970) Stereoscopic vision in macaque monkey: cells sensitive to binocular depth in area 18 of the macaque monkey cortex. Nature 225:41–42

Humayun MS et al (2003) Visual perception in a blind subject with a chronic microelectronic retinal prosthesis. Vis Res 43(24):2573–2581

Johnson RP (1990) Contrast based edge detection. Pattern Recognit 23(3–4):311–318

Kaye SB et al (1999) Monocular and binocular depth discrimination thresholds. Optom Vis Sci 76(11):770–782

Kimia B, Frankel I, Popescu AM (2003) Euler spiral for shape completion. Int J Comput Vis 54(1):159–182

Kimmel R, Malladi R, Sochen N (2000) Images as embedded maps and minimal surfaces: movies, color, texture, and volumetric medical images. Int J Comput Vis 39(2):111–129
Kimmel R (2003) Numerical geometry of images: theory, algorithms and applications. Springer, Berlin
Koch C, Mokwa W, Goertz M, Walter P (2008) First results of a study on a completely implanted retinal prosthesis in blind humans. Sensors, 2008 IEEE, IEEE, Lecce, pp 1237–1240. doi:10.1109/ICSENS.2008.4716667
Koenderink JJ, Doorn AJW (1982) The shape of smooth objects and the way contours end. Perception 11(2):129–137
Koenderink JJ, Doorn AJV (1987) Representation of local geometry in the visual system. Biol Cyber 55(6):367–375
Krauskopf J, Mollon JD (1971) The independence of the temporal integration properties of individual chromatic mechanisms in the human eye. J Physiol 219(3):611–623
Kumar T, Glaser DA (1992) Depth discrimination of a line is improved by adding other nearby lines. Vis Res 32(9):1667–1676
Lawlor M, Zucker SW (2013) Third-order edge statistics: contour continuation, curvature, and cortical connections. NIPS, pp 1763–1771
Liu YS, Stevens CF, Sharpee TO (2009) Predictable irregularities in retinal receptive fields. Proc Natl Acad Sci 106(38):16499–16514
Lu ZL, Sperling G (1996) Contrast gain control in first- and second-order motion perception. J Opt Soc Am A 13(12):2305–2318
Mangoubi SS (1979) Noise and thresholds in vision. PhD. Thesis, Technion
Marr D, Hildreth E (1980) Theory of edge detection. Proc R Soc Lond Ser B Biol Sci 207(1167):187–217
Mokhtarian F, Mackworth AK (1992) A theory of multiscale, curvature-based shape representation for planar curves. IEEE Pattern Anal Mach Intell 14(8):789–805
Monroy A et al. (2011) Beyan straight lines—object detection using curvature. ICIP
Ohlson J (1974) Exact dynamics of automatic gain control. IEEE Trans Commun 22(1):72–75
Palanker D: Photovoltaic retinal prosthesis for restoring sight to the blind. http://web.stanford.edu/~palanker/lab/retinalpros.html
Papoulis A (1965) Probability, random variables and stochastic processes. 1st Ed McGraw-Hill Companies
Parent P, Zucker SW (1989) Trace inference, curvature consistency, and curve detection. IEEE Trans Pattern Anal Mach Intell 11(8):823–839
Peli T, Malah D (1982) A study of edge detection algorithms. Comput Gr Image Process 20(1):1–21
Ratliff F (1965) Mach bands: quantitative studies on neural networks in the retina. Holden-Day Inc.
Richards W, Dawson B, Whittington D (1986) Encoding contour shape by curvature extrema. J Opt Soc Am A 3(9):1483–1491
Riggs LA (1973) Curvature as a feature of pattern vision. Science 181(4104):1070–1072
Roberts B, Harris MG, Yates TA (2005) The roles of inducer size and distance in the Ebbinghaus illusion (Titchener circles). Perception 34(7):847–856
Salinas E (2000) Gain modulation: a major computational principle of the central nervous system. Neuron 27(1):15–21
Saucan E, Appelboim E, Zeevi YY (2008) Sampling and reconstruction of surfaces and higher dimensional manifolds. J Math Imaging Vis 30(3):105–123
Schwartz O, Simoncelli EP (2001) Natural signal statistics and sensory gain control. Nat Neurosci 4(8):819–825
Shapley R, Enroth-Cugell C (1984) Visual adaptation and retinal gain controls. Prog Retin Res 3:263–346
Shefer M (1979) AGE-models for retinal signal processing. M.Sc. Thesis, Technion—Israel Institute of Technology
Singh M, Fulvio JM (2005) Visual extrapolation of contour geometry. Proc Natl Acad Sci USA 102(3):939–944
Sit YF, Chen Y, Geisler WS, Miikkulainen R, Seidemann E (2009) Complex dynamics of V1 population responses explained by a simple gain-control model. Neuron 64(6):943–956
Snippe HP, Hateren JH (2007) Dynamics of nonlinear feedback control. Neural Comput 19(5):1179–1214
Sochen N, Zeevi YY (1998) Representation of colored images by manifolds embedded in higher dimensional non-euclidean space. In: IEEE ICIP98
Sperling G (1970) Models of visual adaptation and contrast detection. Percept Psychophys 8(3):143–157
Stromeyer CF, Riggs LA (1974) Curvature detectors in human vision? Science 184(4142):1199–1201
Sutherland NS (1968) Outlines of a theory of visual pattern recognition in animals and man. Proc R Soc Lond Ser B Biol Sci 171(1024):297–317
Tanaka T, Ohnishi N (1997) Painting-like image emphasis based on human vision systems. Comput Gr Forum 16(3):C253–C260
Tran N et al. (2009) A fully flexible stimulator using 65 nm cmos process for 1024-electrode epi-retinal prosthesis. 31st Annual International Conference of the IEEE EMBS, pp 1643–1646
Treisman AM, Gormican S (1988) Feature analysis in early vision: evidence from search asymmetries. Psychol Rev 95(1):15–48
Ullman S, Schechtman G (1982) Adaptation and gain normalization. Proc R Soc Lond Ser B Biol Sci 216(1204):299–313
Wainwright MJ (1999) Visual adaptation as optimal information transmission. Vis Res 39(23):3960–3974
Watt RJ, Andrews DP (1982) Contour curvature analysis: hyperacuities in the discrimination of detailed shape. Vis Res 22(4):449–460
Watt RJ (1984) Further evidence concerning the analysis of curvature in human foveal vision. Vis Res 24(3):251–253
Weltsch-Cohen Y (2002) AGC models for signal processing in the primary visual cortex. M.Sc. Thesis, Technion
Wilson HR, Wilkinson F, Asaad W (1997) Concentric orientation summation in human form vision. Vis Res 37(17):2325–2330
Wolfe JM, Butcher SJ, Lee C, Hyle M (2003) Changing your mind: on the contributions of top-down and bottom-up guidance in visual search for feature singletons. J Exp Hum Percept Perform 29(2):483–502
Yang J et al. (2009) A super low power MICS band receiver in 65 nm CMOS for high resolution epi-retinal prosthesis, pp 435–438
Yen SC, Finkel LH (1998) Extraction of perceptually salient contours by striate cortical networks. Vis Res 38(5):719–741
Zeevi YY, Ginosar R, Hilsenrath O (1995) United States Patent: 5420637—dynamic image representation system, U.S. Patent 542063730
Zeevi YY, Mangoubi SS (1978) Noise suppression in photoreceptors and its relevance to incremental intensity thresholds. J Opt Soc Am 68(12):1772–1776
Zeevi YY, Shefer M (1981) Automatic gain control of signal processing in vision. J Opt Soc Am 71:1556
Zeevi YY, Kronauer ER (1985) Reorganization and diversification of signals in vision. IEEE Trans Syst Man Cybern 15(1):91–101
Zucker SW, David C, Dobbins A, Iverson L (1988) The organization of curve detection: coarse tangent fields and fine spline coverings. Comput Vis Second Int Conf, pp 568–577